Title
Mechanical reliability and durability of SOFC stacks. Part I : Modelling of the effect of operating conditions and design alternatives on the reliability

Journal
International Journal of Hydrogen Energy, 37(11)

ISSN
0360-3199

Authors
Nakajo, Arata
Mueller, Fabian
Brouwer, Jacob
et al.

Publication Date
2012-06-01

DOI
10.1016/j.ijhydene.2012.03.043

Available online at www.sciencedirect.com

SciVerse ScienceDirect

journal homepage: www.elsevier.com/locate/he

Mechanical reliability and durability of SOFC stacks. Part I : Modelling of the effect of operating conditions and design alternatives on the reliability

Arata Nakajo [a,*], *Fabian Mueller* [b], *Jacob Brouwer* [b], *Jan Van herle* [a], *Daniel Favrat* [a]

[a] *Laboratoire d'Energétique Industrielle (LENI), Institut de Génie Mécanique, Ecole Polytechnique Fédérale de Lausanne, 1015 Lausanne, Switzerland*

[b] *National Fuel Cell Research Center, University of California, Irvine, CA, United States*

ARTICLE INFO

Article history:
Received 29 August 2011
Received in revised form
7 March 2012
Accepted 9 March 2012
Available online 20 April 2012

Keywords:
Solid oxide fuel cell
Thermal stresses
Degradation
Creep
Contact analysis

ABSTRACT

Electrochemical and mechanical aspects in solid oxide fuel cell stack must be understood to meet the reliability targets for market implementation. This study presents a stack modelling framework that combines thermo-electrochemical models, including degradation and a contact finite-element thermo-mechanical model. It considers rate-independent plasticity and creep of the component materials and proposes periodic boundary conditions to model the stacking of repeating units. This Part I focuses on the effects of the operating conditions and design alternatives.

In the present conditions, the stresses in both the anode and the cathode contribute to the probability of failure (P_f), which can be lowered by adjusting the operating conditions. The requirements for mechanical reliability are here opposite to those that alleviate electrochemical degradation. Gas-diffusion layers (GDL) and interconnect design alternatives and stacking have a lower impact on the P_f, but affect the contact pressure on the GDLs, which can cause electrical contacting challenges.

1. Introduction

Sufficient mechanical reliability is a major hurdle to overcome for the commercial viability of solid oxide fuel cell (SOFC) devices [1]. Despite the evidence of this shortcoming, structural issues in SOFC stacks are practically solved by progressive design adjustments while efforts to understand the underlying processes have been limited. The need for a more solid, comprehensive and versatile background is now acknowledged, as the SOFC technology approaches market introduction.

Strong coupling between the phenomena characterises the SOFC field. Stack and system design and operation must be integrated with structural and lifetime analysis to meet performance, reliability, durability, versatility and availability requirements, in the view of the lowest price of electricity delivered to the end-user. Numerous trade-offs govern the development of a functional SOFC system. They act at all scales and affect to similar extents the choice of an electrode microstructure and material, and that of a system layout. In a simplified view, the risks of structural failure scale with power density and number of thermal cycles. Effective mitigation requires the precise knowledge of the mechanisms. The detrimental effects of thermal stresses in SOFC stacks are not completely characterised and cannot be reduced to simple indicators [2–5]. The central component, the membrane

* *Corresponding author*. Tel.: +41 21 693 35 05.
E-mail address: arata.nakajo@epfl.ch (A. Nakajo).

0360-3199/$ – see front matter Copyright © 2012, Hydrogen Energy Publications, LLC. Published by Elsevier Ltd. All rights reserved.
doi:10.1016/j.ijhydene.2012.03.043

Nomenclature

Latin letters

E	Young modulus, Pa
E_a	activation energy, J mol^{-1}
h	thickness, m
j	current density, A m^{-2}
k_o	kinetic constant
L	length, m
m	Weibull modulus
m^{crp}	stress exponent
n	porosity
T	temperature, K
U	electric potential, V
u	displacement, m
V_r	reference volume, m^3

Greek letters

ε	strain
ν	Poisson coefficient
σ_Y	elastic limit, Pa

Indices

a	anode
c	cathode
cl	compatibility layer
e	electrolyte
k	material
o	initial, unperturbed or characteristic
p	plastic
red	reduction
THC	thermal cycle

Superscripts

crp	creep
r	master node
s	slave node

Acronyms

BCAS	barium-calcium-aluminosilicate
Cou	counter-flow
Co	co-flow
CTE	coefficient of thermal expansion
FU	fuel utilisation
GDC	gadolinia-doped ceria
GDL	gas diffusion layer
GLS	glass-ceramic sealant
GSKT	compressive gasket tied at the sealing interfaces
GSK	compressive sealing gasket
LSCF	lanthanum strontium cobaltite ferrite
LSM	lanthanum strontium manganite
MEA	membrane electrode assembly
MIC	metallic interconnect
PR	fraction or percentage of methane conversion in the reformer
RT	room temperature
SRU	standard repeating unit
YSZ	yttria-stabilised zirconia

electrode assembly (MEA), is a multilayer device that mechanically and chemically interacts with the other components of a single repeating unit (SRU). During operation, the physico-chemical alterations that arise from the high-temperature and aggressive environment [6–12] affect the mechanical durability [13,14]. Mechanical failures can occur as well during the last manufacturing steps of the stack. The heat-up and sealing procedures generate conditions that are not straightforward to handle from a structural perspective, whereas the stacking of the SRUs affects the reproducibility of the failures and complicates the analysis.

The cracking modes in the MEA layers and at the interfaces depend on the design, which mainly consists in the choice of a supporting layer and materials of suitable coefficient of thermal expansion (CTE). They may evolve during combined cycling and constant operation conditions because of the relaxation of the initial shielding compressive stress in the weakest layers [15,16]. The failure of the MEA usually follows that of the sealant or gas diffusion layers (GDL) because of the altered mechanical interactions and electrochemical behaviour. A loss of gas tightness detrimentally exposes the materials of the cathode (anode) compartment to reducing (oxidising) gases [17]. Unsteady parasitic combustion provokes hot spots [17,18]. Therefore, fracture mechanics approaches have been applied to study the cracking of the glass-ceramic or sealing interfaces, commonly observed during thermal cycling [19,20]. The difficulty to ensure the reproducibility of the mechanical properties of the sealants and GDL materials [21,22] causes uneven gas supply amongst the stacked SRUs, altered electrical contact and partial loss of contact pressure on the compressive gaskets.

Structural issues at the SRU scale are commonly investigated by importing the temperature profile generated by a thermo-electrochemical model in structural analysis tools. The correct handling of the many manufacturing steps of a SOFC stack, i.e. (i) cell sintering, (ii) components assembly and stacking (iii) sealing procedure and (iv) anode reduction, has a strong influence on the stress in operation. Most of the studies at the SRU scale do not include the effect of the curvature of the cell on the interaction with the other components. The studies by Weil at al. [23,24], Jiang et al. [25] and Lin et al. [26] focus on the sealing solutions by comparing bonded compliant seals, glass-ceramics and compressive gaskets. Bonded compliant seals induce a less stringent joining than glass-ceramics during thermal cycles and partially alleviate the mismatch between the thermal expansions of the parts, while providing better sealing performance than compressive gaskets. The study by Selimovic et al. [27] has investigated the stress in a free single planar cell, subjected to steady-state and transient temperature profiles. The use of either ceramic or metallic interconnects affects the magnitude of the stress, due to the different thermal conductivities. Yakabe et al. [28] have computed large stress in lanthanum chromite interconnects during operation, arising from non-uniform thermal and isothermal strains. Similar modelling tools, with a refined description of the geometry, involving contact between the components, or not, have been applied to button cells as well [29–31].

A specificity of modelling of stresses in SOFCs is the stacking of repeating units, be they tubular or planar. The reduction of the thickness of the components, to reduce ohmic losses and materials costs, among other reasons, promotes stacking challenges. Uneven distribution of the assembly load, increased effects of growing oxide scales, difficulties to ensure the reproducibility of the mechanical properties of the stack components or structural instabilities can cause contacting issues and direct or indirect cell failures. Few studies have been carried out on the overall deformation of a SRU embedded in a stack, because the computational demand of contact analysis limits the number of repeating units that can be meshed. Lin et al. [32] have investigated the effect of the stack support conditions with their model of a three-cell short stack meshed with linear continuum shell elements. In the conditions of their simulations, using points, edge or plane support has a small influence on the stress profiles.

The present study comprises two parts that enlarge with structural consideration our previous investigations on the electrochemical degradation at the SRU/stack scale [33–35]. This Part I seeks to determine the influence of the operating conditions on structural issues in SOFC stacks. The focus of Part II [36] is the mechanical degradation during long-term operation and thermal cycling. The framework is a set of existing models. A structural model of a SRU based on planar, anode-supported cells, which considers the interactions between the components and the curvature of the cell [3,4] is extended. Modified periodic boundary conditions model the stacking of the SRUs and the initialisation procedure is adapted to accommodate glass-ceramic sealants. The stresses in the components of a SRU are computed from the temperature profile generated by a thermo-electrochemical model, that includes several degradation phenomena [33,34,37,38]. Operating conditions optimised for the highest electrical efficiency at start and at long-term operation form the basis of the analysis [33]. Investigated technological alternatives comprise: (i) materials, restricted to the type of cathode, sealant and GDL, and (ii) geometry, limited to the thickness of the metallic interconnectors (MIC).

2. Modelling approach

The structural analysis of a SRU in a stack is performed by importing temperature profiles in a numerical tool based on the finite-element method (ABAQUS [39]). The temperature profile is generated by a thermo-electrochemical model implemented in gPROMS [40], an equation-oriented process-modelling tool. The analysis focuses on the planar, intermediate-temperature stack based on anode-supported cells with an active area of 200 cm^2, developed at LENI-EPFL within the European FP6 FlameSOFC project [41,42]. Fig. 1 depicts the SRU geometry. Boundary conditions in both types of models are imposed to simulate a SRU in a stack [3]. The detailed description of the models and database, from which material mechanical properties are extracted are provided in Refs. [3,33,37,38,42]. The following description focuses on the main features and the specific model improvements developed for the present study.

2.1. Thermo-electrochemical model

The SRU model solves the heat and species transport in the in-plane directions (x and y in Fig. 1), which are coupled to a local one-dimensional electrochemical model discretised through the thickness of the cell (z direction in Fig. 1d) [3]. Ref. [37] describes the implementation of the electrochemical model and its calibration on experimental data from two different segmented-cell tests. The electrochemical model considers both ohmic and non-ohmic losses.

- Ohmic losses comprise the ionic resistivity of the MEA, corrected for constriction effects, the electronic resistivity of the MIC, its oxide layer and contact resistance, and a limited electronic conductivity of the electrolyte that induces a small leakage current.
- On the cathode side, a specific modelling approach is used for composite lanthanum strontium manganite and yttria-stabilised zirconia cathode (LSM-YSZ), or single phase lanthanum strontium cobaltite ferrite (LSCF) cathode. In the case of LSM-YSZ cathode, a model of the composite electrode solves in the z-direction the charge balance along with mass transport. The transfer current is computed following the sequence of elementary steps proposed by van Heuveln et al. [43], adapted for a low coverage of adsorbed oxygen species. In the LSCF cathode case, the modelling follows that proposed by Adler et al. [44]. Experimental data from the literature are used to compute the dependence of the equilibrium vacancy concentration on temperature and oxygen partial pressure and surface exchange properties at the pore wall. Direct exchange of vacancies with the electrolyte is assumed [45].
- On the anode side, the dusty-gas model is solved in one-dimension, through the thickness of the support (z-direction), along with the equation of continuity. The steam-methane reforming reaction rate is computed by the kinetic approach of Achenbach and Riensche [46] and the water-gas shift reaction is assumed at equilibrium until the anode/electrolyte interface. Only hydrogen is electrochemically converted at the interface, following the set of elementary steps proposed by Zhu et al. [47].

Electrochemical degradation analysis under practical conditions requires the implementation of:

- *Degradation phenomena in the electrochemical model* (see Ref. [38] for details). The selection considered in this study includes: (i) decrease of ionic conductivity of 8YSZ, (ii) MIC corrosion, (iii) anode nickel particle growth and, (iv) chromium contamination of the LSM-YSZ cathode. The risk of anode reoxidation and start of formation of zirconates in the LSM-YSZ cathode is monitored during the simulations, but the detrimental effect on the cell performance is not included.
- *System consideration in the thermo-electrochemical SRU model* (see Ref. [33]). The addition of (i) the parasitic power consumption of the air blower and of (ii) losses in the inverter allows to capture the key SOFC system efficiency

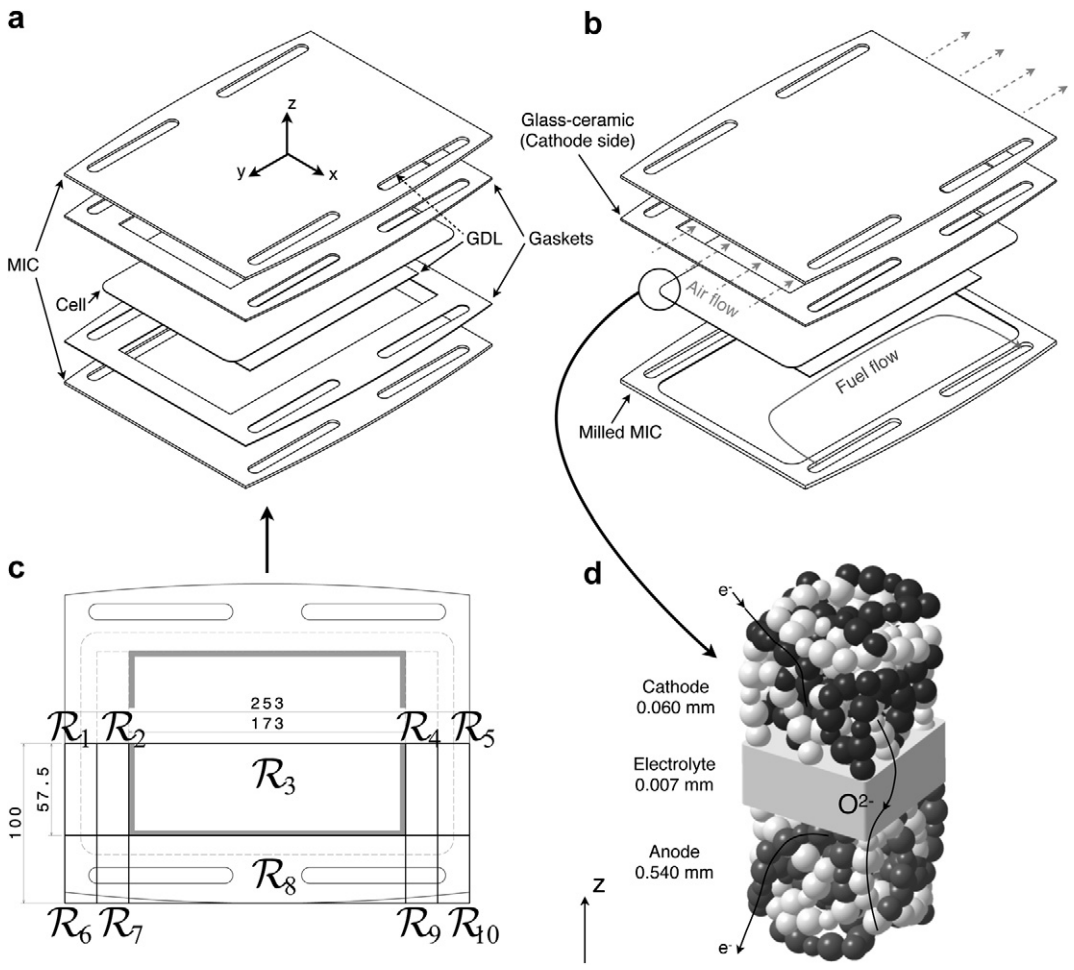

Fig. 1 – View of the FlameSOFC SRU design with (a) compressive gaskets and (b) glass-ceramic sealants. (c) details the domains. (d) provide a schematic view of the MEA in the electrochemical model, for the case of a cell with LSM-YSZ cathode. Indicated gas-flow directions hold for co-flow configuration.

characteristics, while avoiding the burden of a complete integrated system model. This assumes the system is well thermally integrated [47]. Dynamics is restricted to that induced by the degradation processes. Perfect control is applied during degradation simulations to deliver the demanded system electrical power output under fixed air and fuel inlet temperature and composition, fixed maximum SRU temperature and constant fuel utilisation (FU).

2.2. *Structural model*

A static, small deformation, uncoupled contact finite-element thermomechanical model implemented in ABAQUS [39] computes the stresses in the cell layers, MICs, GDLs and sealants. The SRU components depicted in Fig. 1 are meshed and their interactions modelled by the contact algorithm of ABAQUS [39].

2.2.1. *Geometries and mesh*

The SRU geometry slightly differs if compressive gaskets or glass-ceramic sealants are implemented. The modification proposed here is for comparative investigations and not for a design study. Fig. 1a and b show the geometry for the two sealing alternatives. In the case of compressive gaskets, the geometry of the cathode and anode gasket is identical. In the case of glass-ceramic material, only the cathode side sealant is kept, because sealing with the impervious electrolyte is preferable for material compatibility reasons. Therefore, the anode side of the MIC is machined to replace the anode gasket. In reality, additional filler material is needed to maintain the pattern of the anode gas flow.

The dense metallic parts and glass-ceramic sealants are meshed with linear, reduced-integration three-dimensional elements (C3D8R in ABAQUS code terms). Linear special-purpose gasket elements that uncouple the thickness-direction and membrane behaviour (GK3D8R) are used for the compressive gaskets. For the GDL, the results with C3D8R and GK3D8R are compared. The anode support is meshed with second-order three-dimensional reduced-integration solid elements (C3D20R). On the anode front side, the 8YSZ electrolyte, the LSM-YSZ cathode or LSCF cathode and gadolinia-doped ceria (GDC) compatibility layer are added using the skin feature of ABAQUS [39], with second-order reduced-integration shell elements (S8R).

2.2.2. Material mechanical properties

The available data on the mechanical properties of SOFC stack materials is growing, but remains scarce. A linear elastic behaviour is assumed for all ceramic parts. Plasticity with isotropic hardening and von Mises yield criterion is used for the MIC and for GDLs made of metallic foams. The description for compressive sealing gaskets accounts for non-linear response, with differentiated loading and unloading paths, and plasticity. In a first approximation, linear elasticity is completed with creep to model the complex mechanical behaviour of barium-calcium aluminosilicate (BCAS) glass-ceramic sealing material.

The strength of SOFC ceramic materials is not an intrinsic property, but strongly depends on the flaws and defects in the studied volume that result from the manufacturing process and act as stress concentrators. The Weibull analysis [49] provides the assessment of the probability of failure of each MEA layer. It uses the principle of independent action for multi-axial stress loading and a two-parameter Weibull distribution [50] (see e.g. for more details [51]). The provided probabilities of failure are computed for one repeating unit.

The complete set of conditions-dependent mechanical material properties and information needed for the initialisation procedure discussed hereafter is extracted from the compilation in Refs. [42,52]. Table 1 provides the range of the implemented values.

2.2.3. Mechanical interactions between the repeating unit components

Experimental data on the contact behaviour between SOFC materials is very scarce, because they are specific and most of the time proprietary to a stack manufacturer. The limited relative motion of the parts allows use of the surface-to-surface discretisation and the small-sliding tracking approach to reduce the computational time. The contact interactions use a softened contact for the normal behaviour and friction in the tangential direction between the GDL and MIC or cell ($\mathcal{R}_3$ in Fig. 1c). The same approach is applied for the behaviour between the compressive gaskets and the MIC or the cell ($\mathcal{R}_{1,5,6,7,8,9,10}$ in Fig. 1c). In the case of glass-ceramic sealant, or to model tied compressive gaskets (see Section 3), the interactions over the sealing areas $\mathcal{R}_{1,5,6,7,8,9,10}$ is a surface-to-surface tie constraint.

The standard implementation of creep and rate-independent plasticity in solid elements enforces the preservation of the volume [39], which does not completely describe the behaviour of metallic foams and can, combined with a high friction coefficient, overpredict the severity of losses of contact pressure on the GDLs (see Section 4.2). To avoid this shortcoming, the friction coefficient is set at 0.1, which is lower than the value of 0.16 and 0.2 used in [30] and [3,4], respectively. A significant effect on the stress computed in the other SRU component was not observed. Owing to the lack of data on the mechanical properties of SOFC GDL materials and friction coefficients, this assumption does not invalidate the present analysis.

2.2.4. Submodelling

In many anode-supported cell designs, the cathode partially covers the electrolyte. In the design considered in the present study, the cathode covers the domain $\mathcal{R}_3$ indicated by a grey box in Fig. 1c. This requires a dense mesh, which hinders contact simulations. Studies have shown that the cathode has the smallest influence on the curvature of an anode-supported cell, because of its low Young modulus and thickness [16,53]. Therefore, for contact simulations, the cathode is not considered. To overcome this limitation for the assessment of cell failures, the Weibull analysis is performed on a cell submodel with a denser mesh, which includes all cell layers. The displacement boundary conditions computed with the coarser cell mesh in the contact simulations are imposed on the refined cell model through the submodelling capabilities of ABAQUS [39].

2.2.5. Stacking

The modelling of stacking conditions was simplified in our previous studies [3,4]. The flatness of the lower (upper) surface of the bottom (top) MIC was enforced and rotation allowed around the x-axis, except for the lower surface of the bottom MIC (see Fig. 2a). A better approach for repeating units in a large stack and far from the end plates that is used here is to impose modified periodic boundary conditions, using linear multi-point constraints. The periodicity of the in-plane displacement on the identical faces of the MICs is enforced (see Fig. 2b):

$$\begin{aligned} u_1^j - u_1^i &= 0 \\ u_2^j - u_2^i &= 0 \end{aligned} \tag{1}$$

In contrast to the case of a unit cell in a cellular solid [54], the temperature difference over the SRU in operation causes the air exhaust side of a stack operated in co- or counter-flow configuration to expand more than the air inlet one. The linear multi-point constraints implemented in the model approximate the situation. If symmetry along the y-axis is assumed, the difference in displacement along the z-axis between corresponding nodes on the lower and upper meshed MICs, induced by thermal expansion and the assembly load depends on the y-axis:

$$u_3^j - u_3^i - u_3^o(y) = 0 \tag{2}$$

Three fake nodes u^{s1}, u^{s2} and u^r are used to allow for a linear variation of u_3^o and to apply the assembly load:

$$\begin{aligned} & u_3^{s1} + u_3^{s2} - 2u_3^r = 0 \\ & u_3^o(y) = \frac{u_3^{s1}}{2} + \frac{u_3^{s2}}{2} + y \cdot \frac{u_3^{s1} - u_3^{s2}}{2L} \end{aligned} \tag{3}$$

These boundary conditions are applied in this study, because the focus is on the temperature and stress in SRUs in a large stack. Case specific adaptations are required for the SRUs close to the end-plates and depending on the stack design.

2.2.6. Initialisation procedure

Fig. 3 provides a schematic view of the initialisation sequence used to capture correctly the effects of the cell and stack manufacturing steps on the stresses during operation.

Cell sintering. This phase aims at setting in the cell layers the correct residual stresses that arise from the manufacturing of the cell. Because all parts are in contact in the reference state to comply with the use of the small-sliding

Table 1 – Overview of the mechanical properties of the constituents of the SRU, from the data compilation in [42,52].

	T (K)	n (%)	h (m)	ε_{red} (%)	ε_o^p (–)	ε_{THC} (–)	E [c] (GPa)	ν	CTE $\cdot 10^{-6}$ [c] (K^{-1})	k_o^{crp} ($MPa^m\ h^{-1}$)	E_a^{crp} (kJ mol^{-1})	m^{crp}	σ_y (MPa)	σ_o (MPa)	m	$\mathcal{V}_r$ (mm^3)
Cathode	RT	29–30[c]	60e-6	–	0 (C1)	–	41.3	0.28	12.16	5.551e10[i]	392[i]	1.7[i]	–	52	6.7	1.217
(LSM)	1073			–	–	–	48.3	0.28					–	75	3.7	2.836
Cathode	RT	29–30[c]	60e-6	–	−1.25e-7(C2)	–	10[d]	0.32	15.34	5.551e10	392	1.7	–	134[k]	3.8[k]	1.028[k]
(LSCF)	1073			–		–							–	183[k]	5.7[k]	0.575[k]
Electrolyte	RT	0	7e-6	–	−3.16e-4(C1)	–	196.3	0.32	10.21	1.836e07	640	0.5	–	232	5.7	0.535
(YSZ)	1073			–	−3.15e-4(C2)	–	148.6	0.32					–	154	8.6	0.301
Anode	RT	19	542e-6	−0.01	0 (C1)	−2.2e-6	124.9	0.39	12.37	–	–	–	–	–	–	–
(NiO-YSZ)	1073			–	–	–	119.9	0.39					–	–	–	–
Anode	RT	38–40[d]	542e-6	–	–	–	72.5	0.39	12.41	1.040e20	640	2.5	–	79 (73,85)	7 (5,10)	4.812
(Ni-YSZ)	1073			–	–	–	58.1	0.39					–	–	–	–
compat. layer	RT	0	4e-6[l]	–	−2.61e-5(C2)	–	196.3e	0.32	12.63	6.768e04	264	1.0	–	134	3.8	1.028
(GDC)	1073			–		–	148.6[e]	0.32					–	183	5.7	0.575
GDL anode[h]	RT	93	1e-3	–	–	–	0.37	0.3	16.20	7.17e10	284	4.6	0.9	–	–	–
(Ni)	RT	95		–	–	–	0.09	0.3					0.31	–	–	–
	1073	93		–	–	–	0.25	0.3	16.20				0.26	–	–	–
	1073	95		–	–	–	0.06	0.3					0.09	–	–	–
GDL cathode[h,j]	RT	93	2e-3	–	–	–	0.15	0.3	11.80	3.38e13	343.9	4.73	1.27	–	–	–
(Haynes230[a])	RT	95		–	–	–	0.09	0.3					0.92	–	–	–
	1073 K	93		–	–	–	0.12	0.3	11.80				0.88	–	–	–
	1073	95		–	–	–	0.07	0.3					0.63	–	–	–
MIC	RT	0	1.25–2e-3	–	–	–	216.0	0.3	12.80	1.222e06	343.9	4.73	248	–	–	–
(Crofer22APU)[a]	1073 K			–	–	–	65.9	0.3					35	–	–	–
Gasket	RT	na	1–2e-3	–	–	–	0.019[f]	0	10–13.9	–	–	–	–	–	–	–
(Flexitallic 866)[a]	1073			–	–	–							–	–	–	–
Glass-ceramic	RT	0	2e-3	–	–	–	67.4[g]	0.28	11.10	1.627e10	282.9	1.59	43–83	–	–	–
(G18)[b]	1073			–	–	–	14.4[g]	0.28					31–64	–	–	–

a Commercial denominations [61,62].
b BCAS glass.
c Values from RT to 1073 K. Temperature-dependent values implemented in the model.
d Assumed value.
e Values for YSZ.
f Through the thickness: full non-linear pressure-closure relation.
g From stress-strain curves, instead of impulse excitation technique. Arbitrary value of 0.2 GPa before sealing procedure.
h Computed from dense values.
i Values for LSCF.
j CTE of Crofer22APU implemented.
k Values for dense GDC.
l 7 μm in thermo-electrochemical calculations.

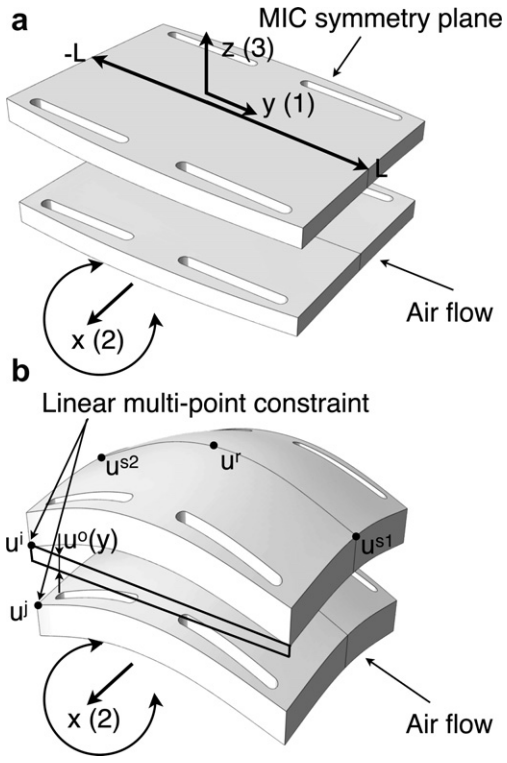

Fig. 2 – Schematic view of the two implemented boundary conditions to represent stacking conditions: (a) enforced flatness of the MIC, (b) modified periodic boundary conditions.

tracking method, relative motion between the cell and the components must be minimized to limit unreal modifications of the contact status at the interfaces. The CTE of the anode, as well as that of the MICs, GDLs and sealants therefore equals

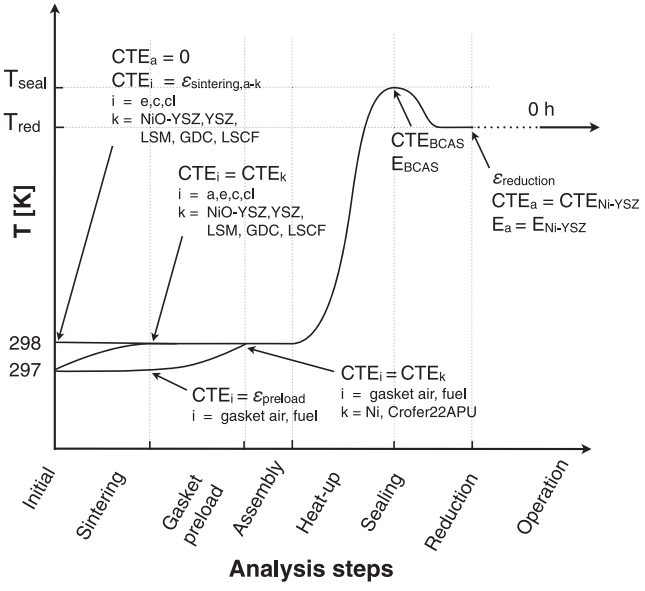

Fig. 3 – Description of the initialisation sequence for contact simulations, i: layer of component, a: anode, e: electrolyte, c: cathode, cl: compatibility layer k: material.

zero during this step, whereas artificial CTEs are applied in the electrolyte, cathode and anode-compensating layer if present. These artificial CTEs correspond to the elastic ($\varepsilon_{sintering}$) and irreversible (ε_0^p) mismatch strains between the anode-support and each other cell layer generated during the cooldown after the sintering, depending on the cell materials and configuration, for an arbitrary small temperature difference of 1 K. They were computed using a simple model based on the Euler–Bernoulli theory [16]. The actual CTEs are then reinserted in the model for the subsequent steps. This is achieved in ABAQUS by controlling the CTEs by a field variable [39], which ensures that the correct residual stress remains in the cell layers throughout the following analysis steps.

Gasket preload. The thickness of the gaskets relative to the GDL can differ before the assembly. This is a design variable, which can be used to control the distribution of the assembly pressure on the SRU. An additional initialisation step is added for this purpose, where an anisotropic and artificial thermal strain is induced prior to the assembly, in a similar manner to the cell sintering step. This step is inactive in the case of a glass-ceramic sealant, because it is expected that the GDLs withstand most of the assembly load during the sealing procedure. From here, the true temperature is used, without correction for modelling purposes.

Sealing procedure. The mechanical properties of glass-ceramic sealant change during the sealing procedure, because of crystallisation. A discrete change in the mechanical properties followed by creep for the desired time period approximates the progressive nature of the process. A low Young's modulus of 200 MPa is arbitrarily used until the end of the sealing procedure. Then the actual mechanical properties of the BCAS glass are set. Annealing at 1073 K for 10 h is performed to relax the stress, before the importation of the temperature profiles generated by the thermo-electrochemical model. The time at which the temperature profiles are imported are referred to as 0 h.

Anode reduction. The modification of the CTE and Young's modulus following the reduction is straightforward to handle. The shrinkage is assumed uniform and contains, because the reference temperature is RT, a correction for the change in CTE of the anode between oxidised and reduced state. It is implemented using the swelling option in ABAQUS [39].

3. Investigated cases

Investigated cases vary in terms of operating conditions and design and modelling alternatives. The focus is on the cell probability of failure and distribution of the contact pressure on the GDL. The contact status at the GDL/cathode interface is investigated, because in anode-supported cells, contacting issues are typically more critical on the cathode side. This is due to the lower electrical conductivity of the materials and lower electrode thickness, which amplifies current constriction issues.

Operating conditions. The case of steam-reformed methane with a carbon ratio of 2 is considered. Our previous study on the effects of the operating conditions on the electrochemical degradation under practical conditions used the present thermo-electrochemical SRU model that is described in

Section 2.1 [33,34]. It forms the basis of the analysis. Previous analyses have demonstrated that SOFC systems for combined heat and power application can have a large system operating envelope with sufficient heat integration for air preheating and fuel processing [48]. Because of the difficulty to include consistently thermo-electrochemical and mechanical aspects in an optimisation problem, the operating conditions that were anticipated to predominantly influence mechanical failures were varied discretely:

- System specific power computed on the basis of the active area of 200 cm^2 : 0.21 or 0.29 W cm^{-2}.
- Maximum SRU temperature: 1100 K, 1125 K or 1150 K.
- Methane conversion fraction in the reformer (PR): 0.25, 0.50 or 0.99.
- Flow configuration: co- (Co) or counter-flow (Cou).

Each temperature profile is implemented after the initialisation procedure described in Section 2.2. The air inlet temperature, fuel utilisation, air and fuel flows and current density to achieve the highest SOFC system efficiency at start or at long-term operation under the aforementionned conditions were determined in Ref. [33]. The cathode degradation phenomena implemented in the electrochemical model (see Section 2.1 and [38]) are valid for composite LSM-YSZ cathode. LSCF cathodes also suffer from chromium contamination, but the nature of the processes differs [55–58], which is not included in the model. Therefore, in the case of LSM-YSZ cathode, the operating conditions optimised for the best long-term electrical efficiency at constant system specific power are used, whereas in the case of LSCF cathode, only those for the highest electrical efficiency at start are available. Table 2 lists the values of the SRU potential, current density, fuel utilisation, air/fuel ratio and air inlet temperature for the main cases.

Design and modelling alternatives. In the conditions treated here, the counter-flow configuration with the lowest methane conversion in the reformer yields the highest durability. The trend is opposite for the co-flow configuration, though it results in similar lifetimes as those for counter-flow with completely pre-reformed methane [33]. Simulations to highlight the effects of design and modelling alternatives are consequently performed for a maximum allowable SRU temperature of 1125 K and methane conversion fraction of 0.99 (Co) and 0.25 or 0.99 (Cou). Design alternatives are:

- Choice of the anode-supported cell: standard Ni-YSZ/YSZ/LSM-YSZ (C1) or LSCF cathode-based cell Ni-YSZ/YSZ/GDC/LSCF (C2). Table 1 lists the thicknesses.
- Sealing solution: compressive gaskets (GSK), compressive gaskets tied at the sealing interfaces (GSKT) or glass-ceramic sealant (GLS). Compressive gaskets are 5% thicker than the GDLs to avoid the release of the contact pressure on the compressive gaskets [4]. The assembly load applied in the simulations is 0.11 MPa and 0.022 MPa, on the basis of the MIC area, for GSK and GLS, respectively. In the GLS case, the temperature profile is applied after the 10 h of annealing at a uniform temperature of 1073 K. The effect of creep relaxation in the glass-ceramic sealant, MICs and GDL for another 10 h is then investigated.
- Thickness of the MICs: 2.0 (standard) or 1.25 mm.
- Mechanical properties of the GDL and compressive gaskets: the GDL relative density is 7% (standard) or 5% (see Table 1). It is combined in the last case to a stress at maximum closure of one half of the nominal case for the through-the-thickness behaviour of the gaskets.

The calculation of the temperature profile accounts for difference in performance between LSM-YSZ and LSCF cathodes. In all thermo-electrochemical calculations, the MIC thickness is 2 mm and the sealing solution is assumed gas-tight.

Modelling alternatives are:

- Elements for the GDL meshes: special-purpose gasket (GK3D8R) (standard), or solid elements (C3D8R).
- Boundary conditions: modified periodic (standard) or enforced flatness of the MICs.

4. Results and discussion

Fig. 4 provides an overview of the effect of (a) the temperature profile on (b) the distribution of tensile first principal stress in the anode and (c) cathode, (d) the contact pressure on the cathode GDL and contact pressure on the cathode

Table 2 – Overview of the main operating conditions for the thermo-electrochemical simulations, from [33,34].

	PR	Sys. spec. Power	Cell	U (V)		j (A cm^{-2})		FU[a]		Air ratio		$T_{air_{inlet}}$ (K)[a]	
				1125 K	1150 K	1125 K	1150 K	1125 K	1150 K	1125 K	1150 K	1125 K	1150 K
Co	0.99	0.21	C1	0.75	0.75	0.30	0.30	0.9	0.91	7.8	5.8	962	930
		0.29	C1	0.71	0.74	0.45	0.44	0.86	0.86	9.3	7.5	985	988
			C2	0.75		0.44		0.9		7.9		964	
Cou	0.25	0.21	C1	0.77	0.77	0.29	0.29	0.9	0.9	5.3	4.3	940	925
		0.29	C1	0.73	0.74	0.44	0.44	0.84	0.88	6.5	5.9	975	975
			C2	0.74		0.44		0.9		6.4		963	
Cou	0.99	0.21	C1	0.77	0.77	0.29	0.29	0.90	0.90	8.4	7.3	957	955
		0.29	C1	0.73	0.74	0.45	0.44	0.84	0.89	9.9	8.8	987	987
			C2	0.76		0.44		0.89		9.8		983	

a Constant during long-term operation.

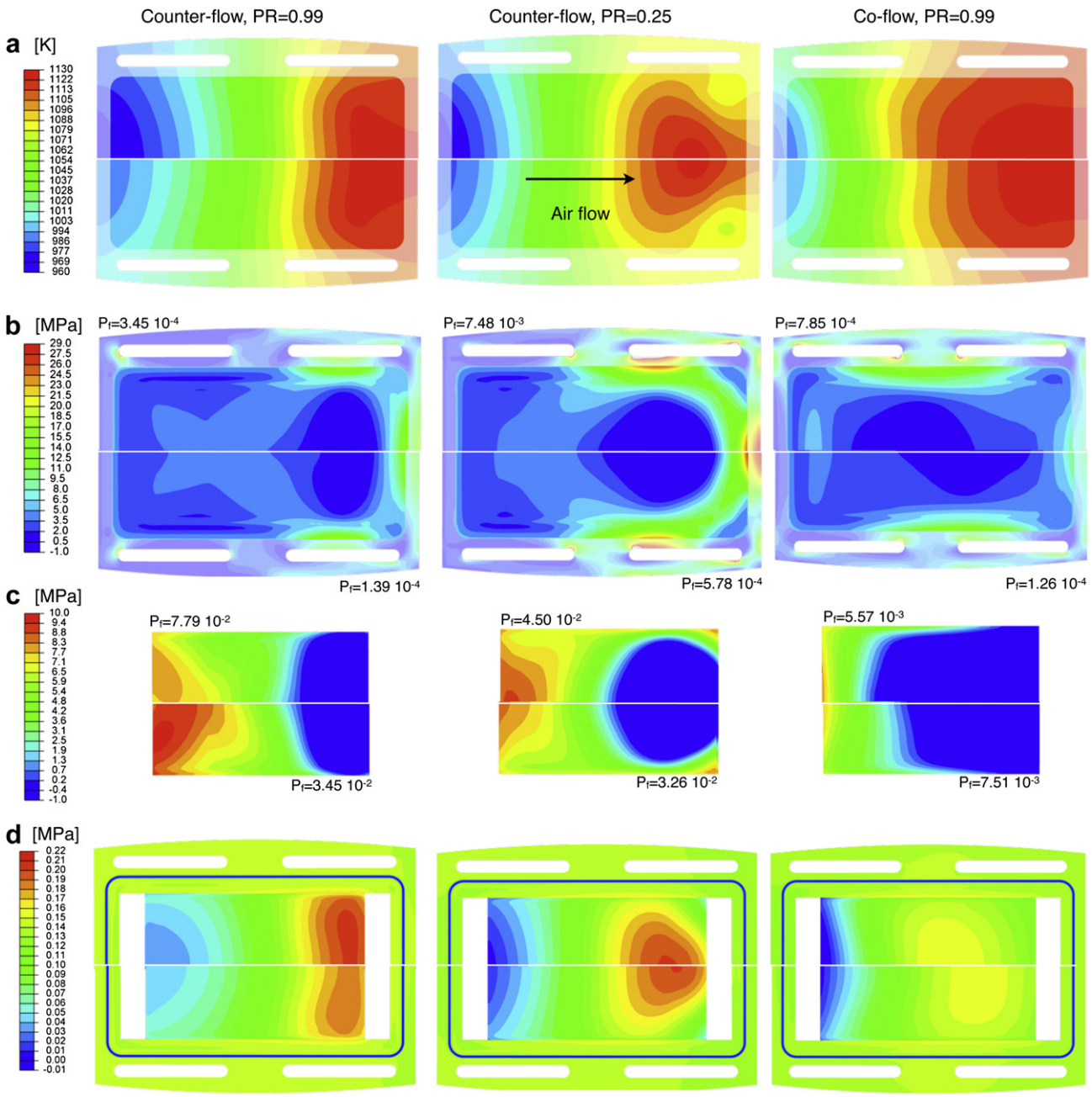

Fig. 4 – (a) Temperature profile and (b) first principal stress in the anode with the MIC displayed in transparency. (c) First principal stress in the cathode and (d) contact pressure on the cathode GDL and compressive gasket. Profiles above (below) the symmetry line correspond to a system specific power of 0.21 (0.29) W cm^{-2}. C1 cell, GSK sealing solution, maximum SRU temperature of 1125 K and MIC thickness of 2 mm.

compressive gasket and GDL, which will be discussed in more detail in the next sections. These results illustrate the case of C1 cell (LSM-YSZ cathode) and compressive gaskets (GSK).

Changing the system specific power from 0.21 W cm^{-2} to 0.29 W cm^{-2} does not modify the trends for a given flow configuration, methane conversion fraction in the reformer and maximum SRU solids temperature. The electrolyte withstands compressive stress in all simulated cases, comprised within approximately 90–140 MPa (not depicted). The zone of highest temperature provokes tensile stress in the anode on the lateral and air outlet sides. This pattern is the most pronounced in the counter-flow configuration with a methane conversion fraction of 0.25, because of the lateral fuel feeding, that cools the fuel inlet zone of $\mathcal{R}_4$ (Fig. 1c) and concentrates the current density at the symmetry line on the air outlet side [34]. For a fixed methane conversion fraction of 0.99 in the reformer, the zone of higher temperature is spread over a larger area of the active area in co-flow than in counter-flow. Indeed, in co-flow configuration, the trade-off between temperature and lean fuel mixture governs the location of the

zone of highest current density, whereas in counter-flow, high temperature and hydrogen-rich fuel mixture available at the air outlet side of the active area promote the electrochemical reactions at this location. The magnitude of the stress is consequently lower in co-flow, but the extent of the high stress zone is larger than in counter-flow configuration, which accounts for the similar anode probability of failures (1.39×10^{-4} and 1.26×10^{-4} in counter, respectively co-flow, at 0.29 W cm^{-2}).

The stress state in the LSM-YSZ cathode is either tensile or compressive, depending on the temperature. The stress fields depicted in Fig. 4 comply with the previous study [16], where the tensile residual stresses reach their maximum around 973 K, because of the temperature dependence of the layers CTE. The transitions between compressive and tensile stresses are around 573 K and 1073 K. The high temperature zone is subjected to compressive stress, except in the counter-flow configuration and for a methane conversion fraction of 0.25 in the reformer, since the zone of highest temperature induces tensile stress *at the edge between the cathode and the gasket*. Deleterious tensile stresses develop in the zone of lower temperature. The identification of the most favourable flow configuration and methane conversion fraction in the reformer requires a Weibull analysis, which is provided in Section 4.1.

The distribution of the contact pressure is even on the cathode compressive gasket, exceeding 0.12 MPa over most of the area, except in the tolerance gap that surrounds the cell. In contrast, the temperature profile significantly affects the contact pressure on the cathode GDL. The counter-flow configuration yields the highest maximum contact pressure, but, with a methane conversion fraction of 0.99 in the reformer, limits the reduction of the contact pressure on the GDL near the air inlet zone. This reduction arises because in the air inlet zone of the SRU, the temperature is higher near the fuel manifold holes than in the active area.

4.1. *Influence of the operating conditions on cell failure and loss of electrical contact*

The analysis presented in Fig. 4 foreshadows an opposite effect of the maximum SRU temperature on the probability of failure of the anode and the LSM-YSZ cathode. The set of Weibull parameters for the strength of the anode that is the closest to the case treated in the electrochemical degradation simulations was selected for this study. The predicted probabilities of failure are low for multiple reasons. The analysis performed in Ref. [3] has shown that (i) uncertainty in the available data on the Weibull parameters of the anode (see Table 1) induces inaccuracy that can exceed an order of magnitude and that (ii) achievable material improvements, such as a Weibull modulus exceeding 10 combined with a characteristic strength of 90 MPa in similar strength test conditions, provide a sufficient reliability for a prototype (10^{-2} for a 50 cell stack). State-of-the-art anodes may have already reached this target, which lies within the 95% confidence interval of the anode data used here and obtained with 15 disk samples only. Furthermore, data on the strength of Ni-YSZ in reduced state and at SOFC operating temperature is limited [52]. The measurements by Malzbender et al. [59] suggest that the decrease of the characteristic strength at high temperature is in the range of 30%, compared with that at room temperature. However, this temperature dependence likely strongly depends on the microstructure and manufacturing procedures. Therefore, the same values measured at room temperature have been used in the present analysis. The confidence intervals for the Weibull parameters of the cathode material are not available.

This study analyses the failures of the two electrodes separately, because discrimination between the most probable failures between the two electrodes, and consequently the assessment of the overall probability of failure, cannot be performed completely reliably with the available data. The emphasis is on the integrity of the anode support. However, more detailed investigations should examine whether or not cracks in the cathode of anode-supported cells can indirectly promote severe mechanical failures. For instance, cracks in the cathode can affect the electrochemical performance, consequently the temperature profile and, depending on the pattern, may further propagate in the electrolyte [60]. This can lead to anode reoxidation and/or cathode reduction, with harmful consequences on the structural integrity of the cell.

Fig. 5a highlights the effect of (i) the maximum allowable SRU solids temperature and (ii) the system specific power on the anode and cathode probability of failure. That of the anode scales with (i), and inversely with (ii). It varies by up to one order of magnitude for a change in maximum SRU temperature from 1100 K to 1150 K. The temperature difference over a SRU is an unreliable indicator for design evaluation [3], but can be used with extreme care. It correctly captures the trends for the anode probability of failure, whereas the dependence for that of the cathode is opposite. The increase of the maximum SRU temperature causes a higher temperature difference over the SRU, because the air inlet temperature optimised in Ref. [33] in the view of the highest system efficiency at long-term operation, and does not vary accordingly (see Table 2). The dependence on the system specific power also arises from the results of the optimisation of the electrical efficiency at long-term operation. In the conditions treated here, the optimised value of the air inlet temperature is governed by trade-offs between cathode overpotential, inlet partial pressure of volatile chromium contaminating species and the need to keep the parasitic air blower power consumption low. Indeed, as the electrochemical performance decreases with time, the current density and air ratio must be ever increased in an accelerated manner to maintain together the fixed system specific power demand and maximum allowable SRU temperature limit, as shown in Fig. 6. The optimiser favours a decrease of the air inlet temperature, and consequently higher temperature differences over the SRU at lower system specific power [34]. Another drawback for mechanical reliability that can limit the benefit of operating at a lower specific power to alleviate electrochemical degradation is the need to adapt accordingly the number of elements in the stack to achieve the specified system power. The larger volume of brittle ceramic material affects the overall probability of failure of the cell. The difficulty to ensure the reproducibility of the material mechanical properties and dimensional tolerances increases, which can promote contacting and gas-distribution challenges.

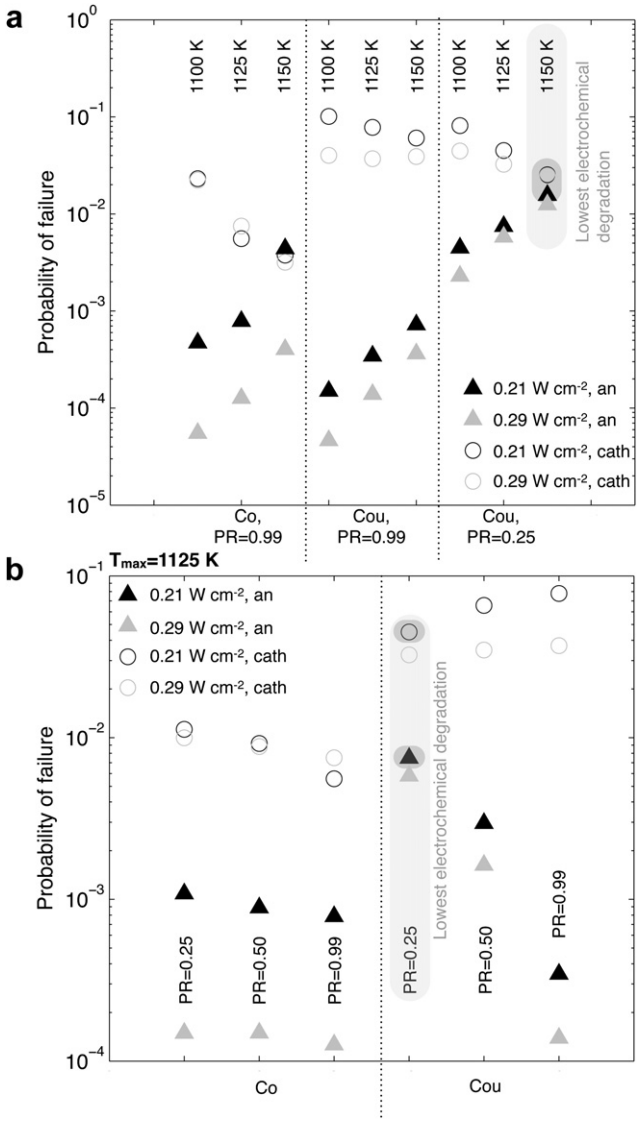

Fig. 5 – (a) Dependence of the anode and cathode probabilities of failure on the maximum SRU temperature and (b) on the methane conversion fraction in the reformer, for the co- and counter-flow configuration. The system specific power is 0.21, 0.25 or 0.29 W cm^{-2} and MIC thickness is 2 mm. The conditions that provide the highest lifetime are indicated in grey (see Table 3 for details).

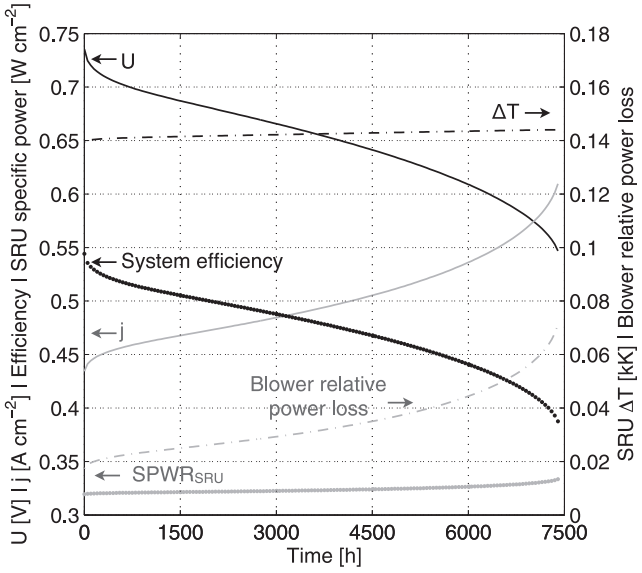

Fig. 6 – Typical evolution during operation at constant system power, of the system efficiency, SRU potential (left), current density (left), SRU specific power (left), temperature difference over the SRU (right) and relative blower power consumption as a fraction of stack power (right). Counter-flow, maximum SRU temperature of 1125 K, PR = 0.25 and system specific power of 0.29 W cm^{-2}.

Fig. 5b shows that the methane conversion fraction in the reformer differently affects the anode probability of failure in co- and counter-flow. For fully pre-reformed methane, the counter-flow configuration is favourable for the anode integrity, but the anode probability of failure strongly increases for higher extent of internal reforming. The co-flow configuration is less affected, because the optimisation of the air inlet temperature in the view of the highest system efficiency at long-term operation increases with amount of internal reforming, up to approximately 1030 K. This air inlet temperature increase alleviate a severe drop of the cell performance near the air inlet, induced by the simultaneous action of the endothermic steam-methane reforming reaction and of air cooling [34].

The probability of failure of the cathode exhibits opposite trends (see Fig. 5b), since it is governed by the aforementioned temperature dependence of the CTEs of the MEA, consequently by the volume of cathode material subjected to temperatures within approx. 573 K–1073 K. Cathode probability of failure exceeds that of the anode, but the uncertainty on the strength of functional LSM-YSZ cathodes affects the accuracy of this prediction. The effect of internal reforming on the temperature profile is beneficial (detrimental) in the counter-flow (co-flow) configuration for the risks of cathode failure.

The effects of the operating conditions on the risks of cell failure depicted in Fig. 5 contrast with the requirements to mitigate electrochemical degradation, which are indicated in grey. Counter-flow combined with a system specific power of 0.21 W cm^{-2}, highest SRU maximum temperature of 1150 K and methane conversion fraction of 0.25 in the reformer yields the highest lifetime and system electrical efficiency (see Table 3), as well as highest anode probability of failure. The anode and cathode probability of failure, as well as lifetime and system electrical efficiency are comparable between co- and counter-flow configurations fed with completely reformed methane. This illustrates the great difficulty to fully optimise a SOFC system under all circumstances. Compromises and design choices have to be made, causing unavoidable limitation either by electrochemical or by thermomechanical degradation effects.

The optimal operating conditions for a cell based on LSM-YSZ (C1) and LSCF (C2) differ and so do the temperature profiles. Fig. 7 depicts three combinations of structural and electrochemical cases to investigate how such a choice impacts the mechanical reliability of the cell. The temperature

Table 3 – Produced electrical energy and averaged system efficiency (inside parentheses) for different flow configurations, system specific powers, maximum SRU temperatures, and methane conversion fractions in the reformer, from Ref. [33].

	Produced energy (kWh cm^{-2}) and (average system efficiency)		
	1100 K	1125 K	1150 K
Co-flow, 0.29 W cm^{-2}, PR = 0.99	0.75 (0.440)	1.23 (0.474)	1.73 (0.493)
Co-flow, 0.21 W cm^{-2}, PR = 0.99	2.08 (0.535)	3.05 (0.542)	4.13 (0.539)
Counter-flow, 0.29 W cm^{-2}, PR = 0.25	0.84 (0.446)	1.42 (0.480)	1.87 (0.506)
Counter-flow, 0.29 W cm^{-2}, PR = 0.99	0.65 (0.421)	1.20 (0.466)	1.55 (0.495)
Counter-flow, 0.21 W cm^{-2}, PR = 0.25	2.40 (0.545)	3.68 (0.553)	5.00 (0.562)
Counter-flow, 0.21 W cm^{-2}, PR = 0.99	2.08 (0.532)	2.96 (0.547)	3.93 (0.557)

profile generated by a C2 cell is applied to a C2 cell for structural analysis (group A) or C1 (group B) cell for comparison, which enables an evaluation of the only mechanical implications of LSCF and GDC compatibility layer. The case of a C1 cell with the corresponding temperature profile (group C) is added for comparison to assess the effect of the LSCF, compared with LSM-YSZ cathode, on the temperature profiles.

In a C2 cell, the cathode withstands tensile stress up to approximately 22 MPa, whereas the electrolyte and compatibility layer undergo compressive stress, in the range of 80–140 MPa and 50–130 MPa, respectively. Weibull parameters for the strength of LSCF cathode could not be found in the literature, which prevents a direct comparison of the probabilities of failure of LSCF and LSM-YSZ cathodes in Fig. 7. The

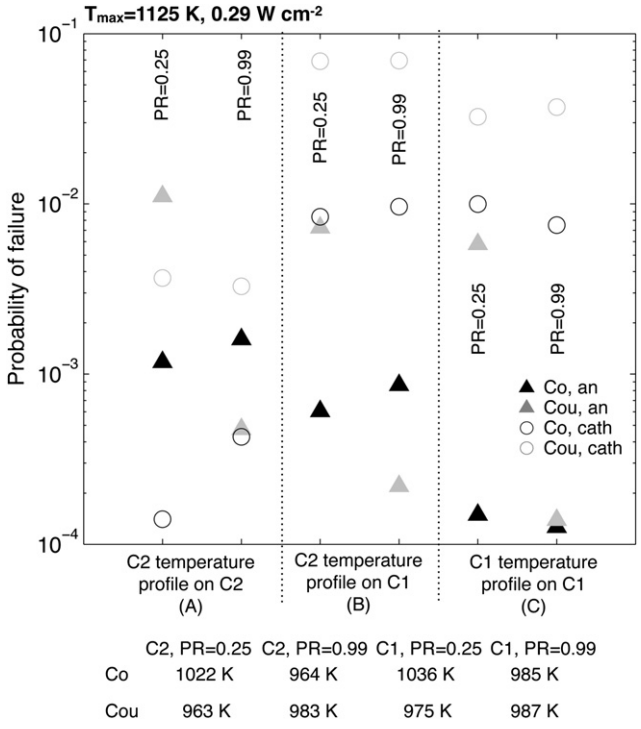

Fig. 7 – Effect of the choice of a cathode material on the anode and cathode probability of failure, for different methane conversion fractions in the reformer and flow configurations. The maximum SRU temperature is 1125 K, the system specific power is 0.29 W cm^{-2}. MIC thickness is 2 mm. The lower table indicates the air inlet temperatures.

GDC compatibility layer needed to prevent chemical reactions between the LSCF cathode and YSZ electrolyte in the C2 cell, increases the anode probability of failure (compare Fig. 7, groups (A) and (B)). In the conditions of the present study, the best use of a LSCF cathode in view of the highest electrical efficiency at start implies a reduction of the air inlet temperature for a given allowable maximum temperature, which affects mechanical reliability.

Table 4 provides the *highest computed* factors on the anode and cathode probability of failure resulting from modifications of the operating conditions. These computed factors are provided to facilitate the comparison between the different simulated cases. Their applicability to any situation is prevented among others by the current limited knowledge of the mechanical properties of SOFC stack materials and by the variety of stack designs and possible SOFC system operation modes.

Fig. 8 depicts (a,b) the vertical displacement of the lower MIC and the cell, together with (c,d) the temperature profile and contact pressure on the cathode GDL, along the symmetry axis. The maximum displacement in the z-direction scales with the allowable maximum SRU temperature and is more pronounced in the co-flow case. This finding suggests that the reduction of the Young modulus of the MIC with temperature exceeds the reduction of residual stress in the cell, which influences the deformation of the SRU. The methane conversion fraction in the reformer has a limited effect in counter-flow. The GDC compatibility layer, combined with the different optimal operating conditions to take advantage of

Table 4 – Computed factors on the anode and cathode probability of failure yielded by modifications of the flow configuration, system specific power, maximum SRU temperature, methane conversion fraction in the reformer (PR) and type of cell, from the data depicted in Figs. 5 and 7. Compressive gaskets, MIC thickness of 2 mm.

	Variation range	Anode	Cathode
Flow configuration[a]	Co to Cou	0.19–1.10	16.1
System specific power	0.29 to 0.21 W cm^{-2}	9.3	0.74–2.51
Maximum SRU temperature	1100 K–1150 K	8.3	0.14
PR	0.99 to 0.25	49.6	0.42–1.73
Cell	LSCF to LSM	0.08	71.1

a For a methane conversion fraction of 0.99 in the reformer.

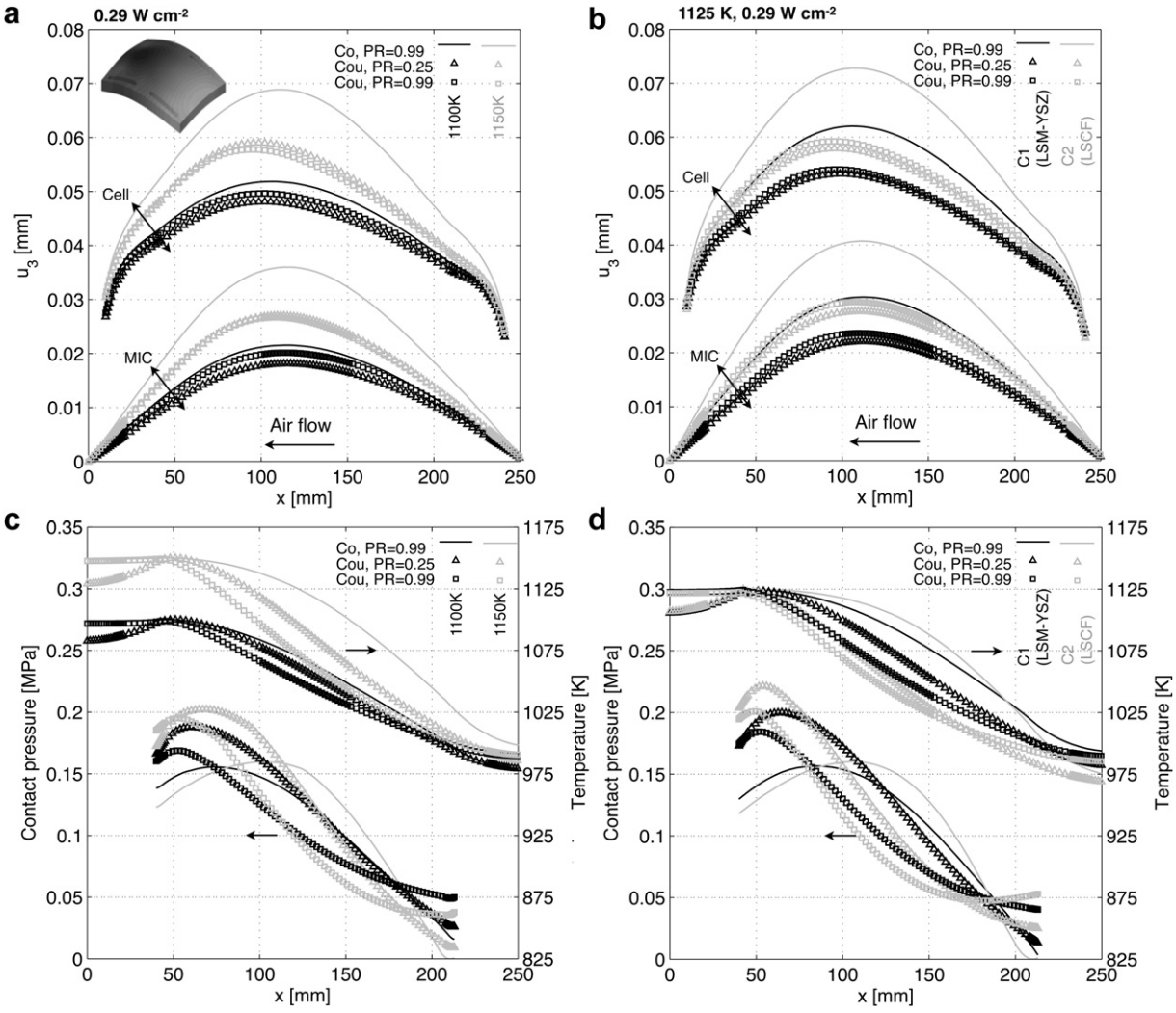

Fig. 8 – (a,b) Displacement along the z-axis of the lower MIC and cell and (c,d) contact pressure on the cathode GDL for the co-flow (PR = 0.99) and counter-flow (PR = 0.25 or PR = 0.99) configuration. (a,c) Effect of maximum SRU allowable temperature, case of LSM-YSZ cathode (C1), (b,d) comparison between C1 and C2 (LSCF with GDC compatibility layer). The curves depicting the displacement of the cell are arbitrarily shifted for display reasons. The insert in (a) illustrate the MIC deflection pattern, amplified by a factor of 2000, observed in all cases. The MIC thickness is 2 mm, and the system specific power is 0.29 W cm^{-2}.

LSCF, amplifies the cell warpage, hence MIC deflection. The maximum value is around 40 μm, which is small compared with the thickness of the GDL layers.

The distribution of the contact pressure on the GDL follows that of the temperature (Fig. 8c and d). The patterns depend mainly on the flow configuration and extent of internal reforming. Variations in system specific power between 0.21 (not depicted) and 0.29 W cm^{-2} do not modify the trends. The contact pressure on the cathode GDL is almost completely relieved in the air inlet zone of the GDL, because of the inverted temperature evolution along the x-axis. In the zone $\mathcal{R}_6$ and $\mathcal{R}_7$ in Fig. 1, qualitatively, the temperature is higher than in $\mathcal{R}_1$ and $\mathcal{R}_2$, because of thermal conduction from the high to the low temperature in the sealing areas $\mathcal{R}_6$–$\mathcal{R}_{10}$, as shown by the temperature profiles depicted in Fig. 4.

4.2. *Effect of the gas diffusion layer, interactions at the sealing interfaces and metallic interconnect on cell failure and loss of electrical contact*

A modification of the mechanical properties of the GDL and gasket materials, MIC thickness or stacking boundary conditions, *within the range or among the types described in* Section 3, has a lower impact on the anode and cathode probability of failure than the adjustment of the operating conditions investigated in the previous section. The computed factors listed in Table 5 range from 0.85 to 1.23, whereas those in Table 4 cover more than one order of magnitude. A change of tens or so micrometers in cell deflection, typically observed in the present study, contributes significantly less to the probability of failure than the thermal and residual stresses.

Table 5 – Computed factors on the anode and cathode probability of failure yielded by modifications of the GDL, MIC thickness, mechanical interaction between the cell and the compressive gasket and boundary conditions, compared with the standard case. C1 cell.

	Anode	Cathode
Flat MICs	0.85	1.09
Compliant GDLs	0.97–1.23	1.08
GDLs meshed with C3D8R	1.07	0.91
MIC = 1.25 mm	0.98	1.08
Gsk, tied	7.66×10^{-4}	2.17×10^{-6}

A higher compliance of the GDLs and gaskets is not necessarily beneficial for the anode integrity, whereas a constraint on the MIC flatness slightly underestimates the anode probability of failure. Meshing the GDLs with solid, instead of special purpose gasket elements does not drastically modify the predictions.

The mechanical interaction between the SRU components increases if contacting pastes are applied between the components. An extreme case is treated here, i.e., the anode and cathode compressive gaskets are tied to the cell and the MICs at their interfaces. The CTE mismatch between the anode (Ni-YSZ: 12.4×10^{-6} K^{-1} between RT and 1123 K) and the MICs (Crofer22APU: 12.0×10^{-6} K^{-1} between RT and 1123 K) alleviates tensile stresses in the MEA, compared with the case where it is partially accommodated by sliding. The anode and cathode probability of failure are drastically reduced (Table 5, Gsk, tied). This beneficial effect may not prevail for all designs. An increase of the mechanical interactions between the components can be either beneficial or detrimental, depending on the mechanical properties of the SRU components.

The distribution of the contact pressure, as well as the cell and MIC vertical deflection are significantly influenced by the mechanical properties of the GDLs and gaskets and stacking boundary conditions. They are comparatively less modified by

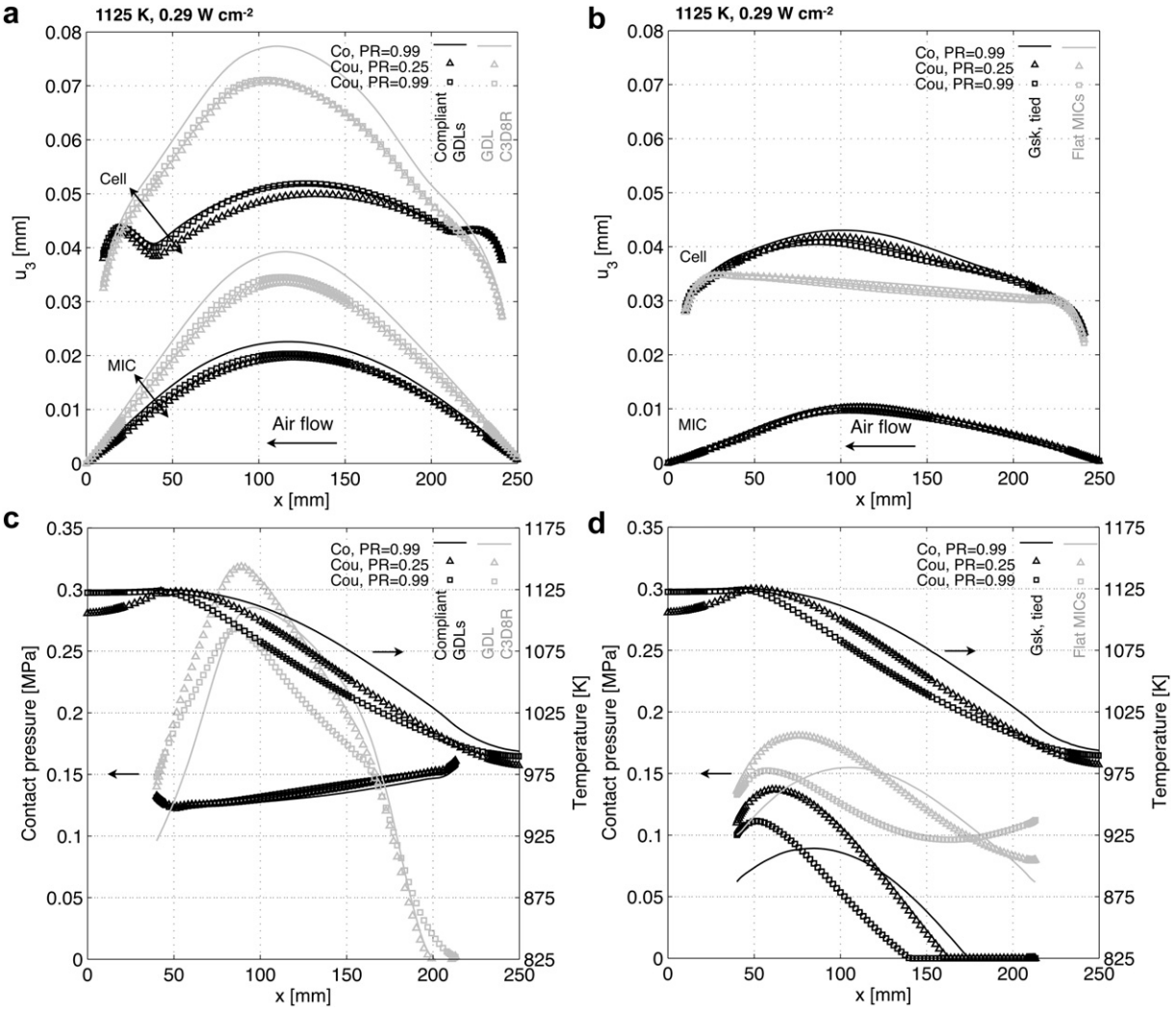

Fig. 9 – (a,b) Displacement along the z-axis of the lower MIC and cell and (c,d) contact pressure on the cathode GDL for the co-flow (PR = 0.99) and counter-flow (PR = 0.25 or PR = 0.99) configuration. (a,b) Impact of the GDL mechanical properties: choice of the GDL elements (C3D8R or GK3D83) and GDL and gasket mechanical properties (relative density of the GDL of 7% or 5% combined to more compliant gaskets). (b,d) Effect of mechanical interaction type between the cell and the compressive gaskets and modelling of stacking conditions. The curves depicting the displacement of the cell are arbitrarily shifted for display reasons. The MIC thickness is 2 mm and the system specific power is 0.29 W cm^{-2}.

changes in the system specific power and maximum SRU temperature. A more compliant gaskets accommodates to a larger extent the cell deformation in the sealing area (see Fig. 9a). Nickel foam with a relative density of 5% exhibits equivalent plastic strains that reach 2.2% in the high temperature zone, whereas on the cathode side the deformation is elastic. This results in lower vertical deflections and different deformation of the cell.

Fig. 9c shows that the contact pressure on the GDL flattens and is the highest in the colder zone, where less plastic deformation develops. This advantage may not be preserved during load following or thermal cycling conditions. Despite the limited maximum equivalent plastic strain in the anode GDL, which does not exceed 0.5% in Fig. 9a,c, the use of solid elements to mesh the GDL and the implementation of Poisson's coefficient modifies the predicted distribution of the contact pressure. The size of the area located at the air inlet side, where the contact pressure is lost, increases (compare with Fig. 8d).

Tied gaskets also increase the extent of the zone affected by loss of contact pressure (Fig. 9b,d). Modelling the stacking conditions by enforcing the flatness of the MIC, instead of modified periodic conditions, yields a more uniform contact pressure distribution on the cathode GDL and limits the cell deflection.

The variety in the calculated distribution of contact pressure, for a single design with small material and operating conditions variations, is in line with the difficulty encountered during the development of a SOFC stack. A refinement of the knowledge on the mechanical behaviour of the interfaces is crucial to study in detail local alterations of the electrical contact. The use of partially-sintered contacting pastes in practice prevent to draw a direct link between the loss of contact pressure or detachment computed here and increase of the interfacial ohmic resistance.

4.3. *Glass-ceramic sealing solution*

The implementation of glass-ceramic sealing material induces a strong history-dependence in the behaviour. Fig. 10 compares the first principal stress in the glass-ceramic sealant and anode support, right after importation of the temperature profile (0 h), and after 10 h, during which the temperature profile of operation is kept constant. Fig. 11 provides the corresponding evolution of the maximum tensile stress in the sealant, von Mises stress in the MIC and anode probability of failure.

The highest maximum first principal stress in the glass-ceramic sealant at 0 h is located in the zones sandwiched between the MICs and where the temperature difference with the annealing temperature of 1073 K is the largest, i.e. air inlet and outlet, close to the symmetry axis, because of the temperature-dependent Young's modulus and mismatch between the CTEs of the glass-ceramic sealant and MIC. The maximum value exceeds that after 10 h of annealing at 1073 K. The strength of the glass-ceramic material at high temperature is in the range of 31–64 MPa, depending on the treatment, but is likely statistically distributed. The maximum first

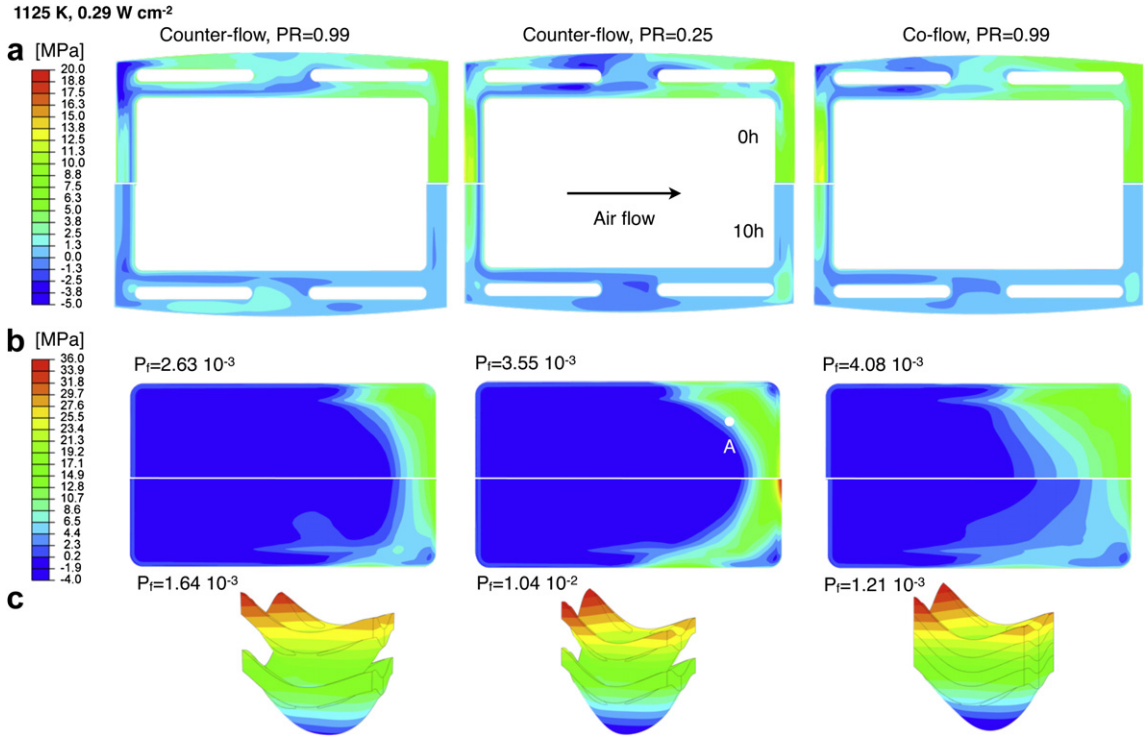

Fig. 10 – (a) Distribution of first principal stress in the glass-ceramic sealant and (b) anode support and (c) qualitative view (amplification factor of 2000) of the MIC deformation (c). The profiles above the symmetry line correspond to 0 h (after an annealing time of 10 h at a uniform temperature of 1073 K, see Section 3). Those below the symmetry line to 10 h, under the temperature profiles depicted in Fig. 4. The maximum temperature is 1125 K, the system specific power is 0.29 W cm^{-2} and the MIC thickness is 2 mm.

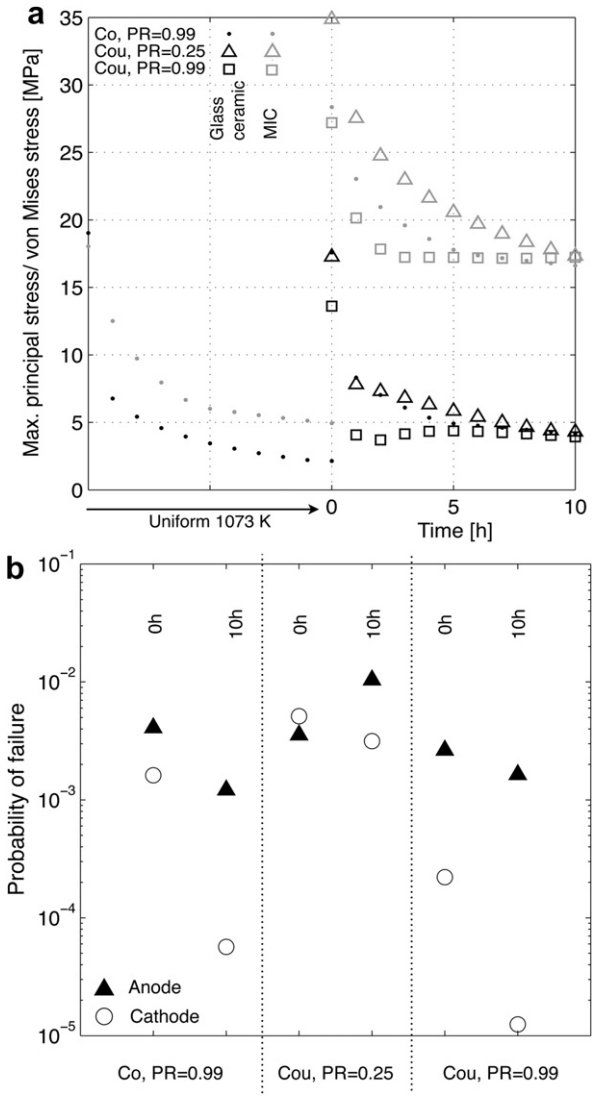

Fig. 11 – (a) Evolution of the maximum first principal stress in the anode and von Mises stress in the MIC, during the period of 10 h under the temperature profile of operation. (b) Anode and cathode probabilities of failure, at 0 h (after annealing during 10 h at a uniform temperature of 1073 K, see Section 3) and after 10 h. The maximum temperature is 1125 K, the system specific power is 0.29 W cm^{-2} and the MIC thickness is 2 mm.

principal stress depicted in Fig. 10 exceeds 15 MPa and may cause high risks of cracking.

In operation, creep proceeds in the MIC, GDLs and glass-ceramic sealant. The stress in the sealant is relieved faster in the zones subjected to higher temperature and higher stress. Most of the decay occurs within 5 h. The maximum von Mises stress in the MIC evolves in a similar way.

The anode stress distributions shown in Fig. 10 arise from the temperature dependent mismatch between the anode and the MICs, which is more pronounced in the temperature range from 973 to 1073 K (Crofer22APU: 11.6 $\times$ 10^{-6} K^{-1}, Ni-YSZ: 12.4 $\times$ 10^{-6} K^{-1} in average) than at higher temperature (Crofer22APU: 12.0 $\times$ 10^{-6} K^{-1} at 1123 K). Compressive stresses protect the anode in the lower temperature region, until the first half of the SRU from the air inlet side, whereas tensile stresses develop in the zones of higher temperature. For comparison, the anode probability of failure after 10 h of annealing at 1073 K is 9.79 $\times$ 10^{-8}. As is anticipated by the observation of Fig. 10, the probability of failure is initially the highest in co-flow. In counter-flow, it is the highest (lowest) with a methane conversion fraction of 0.25 (0.99).

Ageing during 10 h after the temperature profile of operation is applied noticeably reduces the magnitude of the stress for completely pre-reformed methane. The anode probability of failure consequently decreases by a factor of 3.4 and 1.6 in co- and counter-flow, respectively. In contrast, the stress in the anode increases at the air outlet side, at the symmetry axis, in counter-flow combined with a methane conversion fraction of 0.25. Part II of this study [36] shows that in the long-term, the anode stress distribution tends towards that predicted for the case of compressive gaskets. This first increase by a factor of 2.9 is therefore a short-term maximum.

Tensile stress up to 11–13 MPa develops in the cathode only close to its air outlet side corners (location A in Fig. 10, stress profiles not depicted). The evolution of the cathode probability of failure is opposite to that of the anode. It first decreases, by a factor of 28.6 and 1.63 within 10 h, in co-flow with completely reformed methane and counter-flow with a methane conversion fraction of 0.25, respectively. It then increases in the long-term and exceeds the value at 0 h (see Part II).

The reduction of the anode, which is commonly performed when hydrogen is fed for the first time in the stack, restricts the pre-selection of cells to circumvent assembly issues. Proof-testing procedures can nevertheless assist stack commissioning before system implementation. Here, the history-dependent behaviour of a SOFC stack with glass-ceramic sealants drastically complicates the determination of the relevant test conditions, be it for the cell or the sealant.

The stronger mechanical interactions at the sealing interfaces, which partially cover the MICs and electrolyte, induce a more complex deformation of the SRU than in the GSK case (compare insert in Figs. 8a and 10c). Fig. 12a shows that the vertical displacement along the y-axis is inverted, because of the increased dissymmetry in the z direction induced by the implementation of the glass-ceramic sealant in the SRU design considered here (Fig. 1b). The cell and MIC deflections are very similar at 0 h for all operating conditions. The maximum values is 43 μm, which is slightly higher than the GSK case. After 10 h, the maximum value increases and the patterns differ because of the temperature profiles.

The assembly load in the GLS case is 0.11 and 0.022 MPa on the basis of the SRU footprint area in the GSK case. In contrast, the contact pressure on the GDL is higher in the former case, and does not vanish at the air inlet side (compare Fig. 9c grey curves, and Fig. 12), because the CTE of the glass-ceramic (11.1 $\times$ 10^{-6} K^{-1}, between RT and 1073 K) is lower than that of the GDLs (16.2 $\times$ 10^{-6} K^{-1} and 11.8 $\times$ 10^{-6} K^{-1}). This increases the compressive stress in the GDL layers. The contact pressure on the GDL is therefore predominantly governed by the difference in CTE and mechanical properties between the GDL and the glass-ceramic sealant, rather than the assembly load.

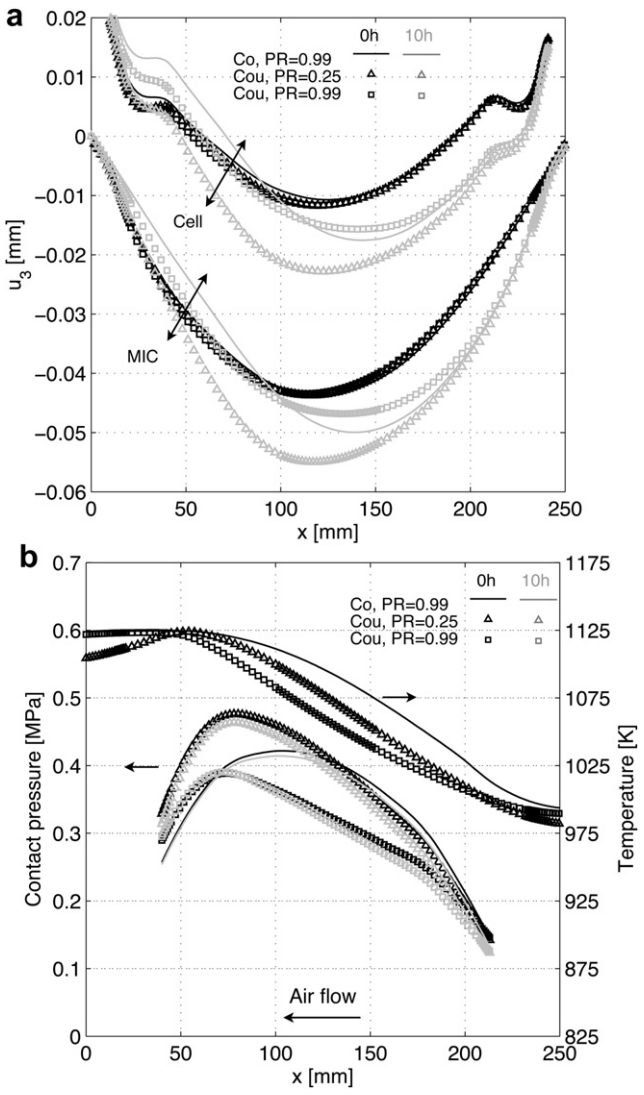

Fig. 12 – (a) Displacement along the z-axis of the MIC and cell and (b) contact pressure on the cathode GDL at 0 h (after annealing during 10 h at a uniform temperature of 1073 K, see Section 3) and after aging during 10 h. The curves depicting the displacement of the cell are arbitrarily shifted for display reasons. The MIC thickness is 2 mm, the maximum SRU temperature is 1125 K and the system specific power is 0.29 W cm^{-2}.

The absence of zones where the contact pressure is lost is at first sight beneficial. Design precautions are however needed to ensure the durability of this advantage. The irreversible deformation due to rate-independent plasticity and creep during prolonged operation can amplify the detrimental effects of thermal and electrical load cycling [36].

5. Conclusion

This study enlarged with structural analysis our previous investigations on the effects of the operating conditions on the initial performance and degradation of a SOFC stack, including system level considerations [33,34].

In the conditions treated here, both the anode and the cathode contribute to the cell probability of failure provided by Weibull analysis. Compressive stress in the range of 90–140 MPa shield the thin electrolyte. The determination of the most critical layer can be calculated, but practically suffers from the large confidence intervals for the Weibull parameters, that cause a scatter in the range of one to several orders of magnitude. The anode probability of failure is predominantly governed by the pattern of the temperature profile, whereas that of the LSM-YSZ cathode depends upon the local CTE mismatch with the other cell layers.

Adjustments of the operating conditions, such as flow configuration, maximum SRU temperature, system specific power and methane conversion fraction in the reformer, can reduce the anode and cathode probability of failure by a factor of approximately 300 and 30, respectively. Counter-flow configuration together with low methane conversion in the reformer, high maximum SRU temperature limit and low system specific power is the most favourable case in the view of electrochemical degradation, because it lowers and flattens the cathode overpotential and minimises the blower parasitic consumption. These requirements do not promote mechanical reliability. Here, pre-reformed anode gas, high system specific power and the lowest SRU temperature limit yield the lowest anode probability of failure. This clearly shows that the best use of the advantages in terms of long-term electrical efficiency provided by these decision variables for the development and operation of a SOFC stack must be balanced with mechanical reliability considerations.

The GDL mechanical properties, MIC thickness and stacking boundary conditions have a lower impact on the layers probability of failure, which is modified by a factor in the range of 0.85–1.23. The effect of level of mechanical interactions between the components and the choice of a sealing solution is, in contrast, significant.

In the case of a glass-ceramic sealant, the cathode and anode probability of failure decrease by more than one order of magnitude during a short annealing period of 10 h, when completely reformed methane is fed in the SRU. In contrast, the anode probability of failure increases in counter-flow together with a methane conversion fraction of 0.25 in the reformer. As is discussed in Part II, the long-term behaviour differs. When the temperature profile of operation is applied, the glass-ceramic sealant is subjected to stress that may cause cracking, but data on the Weibull parameters could not be found for the BCAS sealant. Most of the decay in stress relief occurs within 5 h.

The residual stress in the cell and dissymmetry in the stacked direction are the driving forces for the deflection of a SRU in a stack. In operation, the deflection scales with temperature and depends on the level of mechanical interaction between the components and stacking boundary conditions, because of the temperature dependence of the mechanical properties. The influence on the cell probability of failure is limited, compared with that of the operating conditions. The contact pressure on the cathode GDL in the air inlet zone is significantly relieved in operation in most cases, completely in the case of tied gaskets, which may reflect

possible electrical contacting issues. For glass-ceramic sealants, it is governed by the differences in mechanical properties of the GDL and sealants, rather than by the applied assembly load. More compliant GDLs and compressive gaskets are not necessarily beneficial. They flatten the distribution of the contact pressure, which may however not be preserved in the long term because of the higher plastic deformation and increase the anode probability of failure.

The influence of the temperature profile and strong history-dependence of the risks of failure of the cell, in the case of a glass-ceramic sealant, highlights the crucial importance to investigate in future the transient behaviour during load following scenarii of relevance for practical applications. The analysis shows that the assessment of design and operating conditions options on the basis of fixed conditions and simple indicators, such as temperature difference or thermal gradients provide limited and, in the worst case, possibly misleading insights into the complex trade-offs that characterise the SRU initial and long-term electrochemical behaviour and mechanical reliability. Failure of the cathode is reported in experiments and predicted by the simulation. Stress analyses can therefore not neglect this layer.

Further research is needed to completely understand and quantify the trade-offs between mechanical reliability and electrochemical performance of SOFC stacks. Efforts should be placed on characterising further the mechanical properties of the SOFC stack materials under appropriate conditions. Thorough validation at the stack scale of both thermo-electrochemical and mechanical models is also a prerequisite to provide reliable guidance. The quantitative information generated in the present study, such as the factors on the probability of failure, is therefore for comparison purpose.

Acknowledgements

This work was funded by the Swiss SOFC Consortium, co-financed by the Swiss Federal Office of Energy (SFOE) and Swisselectric Research, contract number 152210, and the FP6 FLAMESOFC European project, contract number CE-Flame SOFC-019875. The authors would like to thank Dr. Cugnoni (LMAF-EPFL) for all his useful advices. Prof. T. Kawada (Tohoku University) is kindly acknowledged for careful reading of the manuscript. gPROMS, a modelling tool from Process System Enterprise (PSE) and ABAQUS from Simulia have been used under academic licencing. Computations have been performed on the Pleiades2 cluster located at EPFL.

REFERENCES

[1] Kuebler J, Vogt UF, Haberstock D, Sfeir J, Mai A, Hocker T, et al. Simulation and validation of thermo-mechanical stresses in planar SOFCs. Fuel Cells 2010;10(6):1066–73.
[2] Fischer K, Seume J. Impact of the temperature profile on thermal stress in a tubular solid oxide fuel cell. Journal of Fuel Cell Science and Technology 2009;6(1):0110171–9.
[3] Nakajo A, Wuillemin Z, Van herle J, Favrat D. Simulation of thermal stresses in anode-supported solid oxide fuel cell stacks. Part I: probability of failure of the cells. Journal of Power Sources 2009;193(1):203–15.
[4] Nakajo A, Wuillemin Z, Van herle J, Favrat D. Simulation of thermal stresses in anode-supported solid oxide fuel cell stacks. Part II: loss of gas-tightness, electrical contact and thermal buckling. Journal of Power Sources 2009;193(1):216–26.
[5] Schuler JA, Tanasini P, Hessler-Wyser A, Van herle J. Rapid chromium quantification in solid oxide fuel cell cathodes. Scripta Materialia 2010;63(8):895–8.
[6] Liu Y, Hagen A, Barfod R, Chen M, Wang H, Poulsen F, et al. Microstructural studies on degradation of interface between LSM-YSZ cathode and YSZ electrolyte in SOFCs. Solid State Ionics 2009;180(23–25):1298–304.
[7] Hagen A, Liu YL, Barfod R, Hendriksen PV. Assessment of the cathode contribution to the degradation of anode-supported solid oxide fuel cells. Journal of the Electrochemical Society 2008;155(10):B1047–52.
[8] Simwonis D, Tietz F, Stöver D. Nickel coarsening in annealed Ni/8YSZ anode substrates for solid oxide fuel cells. Solid State Ionics 2000;132(3–4):241–51.
[9] Menzler NH, de Haart LG, Sebold D. Characterization of cathode chromium incorporation during mid-term stack operation under various operational conditions. ECS Transactions 2007;7(1):245–54.
[10] Holzer L, Münch B, Iwanschitz B, Cantoni M, Hocker T, Graule T. Quantitative relationships between composition, particle size, triple phase boundary length and surface area in nickel-cermet anodes for solid oxide fuel cells. Journal of Power Sources 2011;196(17):7076–89.
[11] Tanasini P, Cannarozzo M, Costamagna P, Faes A, Van herle J, Hessler-Wyser A, et al. Experimental and theoretical investigation of degradation mechanisms by particle coarsening in SOFC electrodes. Fuel Cells 2009;9(5):740–52.
[12] Faes A, Hessler-Wyser A, Presvytes D, Vayenas C, Van herle J. Nickel-zirconia anode degradation and triple phase boundary quantification from microstructural analysis. Fuel Cells 2009;9(6):841–51.
[13] Lara-Curzio E, Radovic M, Trejo M, Cofer C, Watkins T, More K. Effect of thermal cycling and thermal aging on the mechanical properties of, and residual stresses in, Ni-YSZ/YSZ bi-layers. Advances in Solid Oxide Fuel Cells II 2007;27(4):383–91.
[14] Kuebler J, Primas R, Gut B. Mechanical strength of thermally aged and cycled thin zirconia sheets. Advances in Science and Technology 1995:923–8.
[15] Kawada T, Watanabe S, Ichi Hashimoto S, Sakamoto T, Unemoto A, Kurumatani M, et al. Classification of mechanical failure in SOFC and Strategy for evaluation of operational margin. ECS Transactions 2009;25(2):467–72.
[16] Nakajo A, Van herle J, Favrat D. Sensitivity of stresses and failure mechanisms in SOFCs to the mechanical properties and geometry of the constitutive layers. Fuel Cells 2011;11(4):537–52.
[17] Wuillemin Z, Autissier N, Nakajo A, Luong MT, Van herle J, Favrat D. Modeling and study of the influence of sealing on a solid oxide fuel cell. Journal of Fuel Cell Science and Technology 2008;5(1):011016–9.
[18] Faes A, Nakajo A, Hessler-Wyser A, Dubois D, Brisse A, Modena S, et al. Redox study of anode-supported solid oxide fuel cell. Journal of Power Sources 2009;193(1):55–64.
[19] Nguyen B, Koeppel B, Ahzi S, Khaleel M, Prabhakar S. Crack growth in solid oxide fuel cell materials: from disrcete to continuum damage modeling. Journal of the American Ceramic Society 2006;89(4):1358–68.
[20] Müller A, Becker W, Stolten D, Hohe J. A hybrid method to assess interface debonding by finite fracture mechanics. Engineering Fracture Mechanics 2006;73(8):994–1008.

[21] Stephens E, Vetrano J, Koeppel B, Chou Y, Sun X, Khaleel M. Experimental characterization of glass-ceramic seal properties and their constitutive implementation in solid oxide fuel cell stack models. Journal of Power Sources 2009; 193(2):625–31.
[22] Badiche X, Forest S, Guibert T, Bienvenu Y, Bartout JD, Ienny P, et al. Mechanical properties and non-homogeneous deformation of open-cell nickel foams: application of the mechanics of cellular solids and of porous materials. Materials Science and Engineering A 2000;289(1–2):276–88.
[23] Weil K, Koeppel B. Comparative finite element analysis of the stress-strain states in three different bonded solid oxide fuel cell seal designs. Journal of Power Sources 2008;180(1): 343–53.
[24] Weil K, Koeppel B. Thermal stress analysis of the planar SOFC bonded compliant seal design. International Journal of Hydrogen Energy 2008;33(14):3976–90.
[25] Jiang TL, Chen MH. Thermal-stress analyses of an operating planar solid oxide fuel cell with the bonded compliant seal design. International Journal of Hydrogen Energy 2009;34(19): 8223–34.
[26] Lin CK, Huang LH, Chiang LK, Chyou YP. Thermal stress analysis of planar solid oxide fuel cell stacks: effects of sealing design. Journal of Power Sources 2009;192(2): 515–24.
[27] Selimovic A, Kemm M, Torisson T, Assadi M. Steady state and transient thermal stress analysis in planar solid oxide fuel cells. Journal of Power Sources 2005;145(2):463–9.
[28] Yakabe H, Yasuda I. Model analysis of the expansion behavior of $LaCrO_3$ interconnector under solid oxide fuel cell operation. Journal of the Electrochemical Society 2003;150(1): A35–45.
[29] Chiang LK, Liu HC, Shiu YH, Lee CH, Lee RY. Thermal stress and thermo-electrochemical analysis of a planar anode-supported solid oxide fuel cell: effects of anode porosity. Journal of Power Sources 2010;195(7):1895–904.
[30] Chiang LK, Liu HC, Shiu YH, Lee CH, Lee RY. Thermo-electrochemical and thermal stress analysis for an anode-supported SOFC cell. Renewable Energy 2008;33(12):2580–8.
[31] Laurencin J, Delette G, Lefebvre-Joud F, Dupeux M. A numerical tool to estimate sofc mechanical degradation: case of the planar cell configuration. Journal of the European Ceramic Society 2008;28(9):1857–69.
[32] Lin CK, Chen TT, Chyou YP, Chiang LK. Thermal stress analysis of a planar SOFC stack. Journal of Power Sources 2007;164(1):238–51.
[33] Nakajo A, Mueller F, Brouwer J, Van herle J, Favrat D. Progressive activation of degradation processes in SOFC stacks. Part I: Lifetime extension by optimisation of the operating conditions, Journal of Power Sources, in preparation.
[34] Nakajo A, Mueller F, Brouwer J, Van herle J, Favrat D. Progressive activation of degradation processes in SOFC stacks. Part II: Modelling of the spatial distribution of the degradation, Journal of Power Sources, in preparation.
[35] Nakajo A, Mueller F, McLarty D, Brouwer J, Van herle J, Favrat D. The effects of dynamic dispatch on the degradation of solid oxide fuel cell systems. The Journal of the Electrochemical Society 2011;158(11):B1329–40.
[36] Nakajo A, Mueller F, Brouwer J, Van herle J, Favrat D. Mechanical reliability and durability of SOFC stacks. Part II: modelling of mechanical failures during aging and cycling, in preparation.
[37] Nakajo A, Wuillemin Z, Metzger P, Diethelm S, Schiller G, Van herle J, et al. Electrochemical model of solid oxide fuel cell for simulation at the stack scale I. calibration procedure on experimental data. Journal of the Electrochemical Society 2011;158(9):B1083–101.
[38] Nakajo A, Tanasini P, Diethelm S, Van herle J, Favrat D. Electrochemical model of solid oxide fuel cell for simulation at the stack scale II: implementation of degradation processes. Journal of the Electrochemical Society 2011;158(9): B1102–18.
[39] ABAQUS Inc., v6.8, Hibbitt, Karlsson and Sorensen, Rhode Island.
[40] gPROMS (General Process Modelling and Simulation Tool), v3.2, Process Systems Enterprise Ltd., London.
[41] Wuillemin Z. Experimental and modeling investigations on local performance and local degradation in solid oxide fuel cells. Ph.D. thesis; 4525; Lausanne; 2009.
[42] Nakajo A. Thermomechanical and electrochemical in anode-supported solid oxide fuel cell stacks. Ph.D. thesis; 4930; Lausanne; 2011.
[43] van Heuveln FH, Bouwmeester HJM. Electrode Properties of Sr-doped $LaMnO^3$ on yttria-stabilized zirconia. Journal of the Electrochemical Society 1997;144(1):134–40.
[44] Adler SB, Lane JA, Steele BCH. Electrode kinetics of porous mixed-conducting oxygen electrodes. Journal of the Electrochemical Society 1996;143(11):3554–64.
[45] Svensson AM, Sunde S, Nişancioglu K. Mathematical modeling of oxygen exchange and transport in air-Perovskite-Yttria-stabilized zirconia interface regions. Journal of the Electrochemical Society 1998;145(4):1390–400.
[46] Achenbach E, Riensche E. Methane/steam reforming kinetics for solid oxide fuel cells. Journal of Power Sources 1994;52(2): 283–8.
[47] Zhu H, Kee RJ, Janardhanan VM, Deutschmann O, Goodwin DG. Modeling elementary heterogeneous chemistry and electrochemistry in solid-oxide fuel cells. Journal of the Electrochemical Society 2005;152(12):A2427–40.
[48] Mueller F, Jabbari F, Gaynor R, Brouwer J. Novel solid oxide fuel cell system controller for rapid load following. Journal of Power Sources 2007;172(1):308–23.
[49] Weibull W. A statistical theory of the strength of materials. Proceedings of The Royal-Swedish Institute for Engineering Research 1939;151:1–45.
[50] Nakajo A, Stiller C, Härkegård G, Bolland O. Modeling of thermal stresses and probability of survival of tubular SOFC. Journal of Power Sources 2006;158(1):287–94.
[51] Nemeth NN, Bratton RL. Overview of statistical models of fracture for nonirradiated nuclear-graphite components. Nuclear Engineering and Design 2010;240(1):1–29.
[52] Nakajo A, Kübler J, Faes A, Vogt U, Schindler H, Chiang LK, et al. Compilation of mechanical properties for the structural analysis of solid oxide fuel cell stacks. constitutive materials of anode supported cells. Ceramics International 2012;38(5): 3907–27.
[53] Malzbender J, Wakui T, Steinbrech R. Curvature of planar solid oxide fuel cells during sealing and cooling of stacks. Fuel Cells 2006;6(2):123–9.
[54] Galli M., Botsis J., Janczak-Rusch J. An elastoplastic three-dimensional homogenization model for particle reinforced composites. Computational Materials Science.
[55] Konysheva E, Penkalla H, Wessel E, Mertens J, Seeling U, Singheiser L, et al. Chromium poisoning of perovskite cathodes by the ODS alloy $Cr_5FeY_2O_3$ and the high chromium ferritic steel Crofer22APU. Journal of the Electrochemical Society 2006;153(4):A765–73.
[56] Jiang SP, Zhang JP, Apateanu L, Foger K. Deposition of chromium species at Sr-doped $LaMnO_3$ electrodes in solid oxide fuel cells. I. mechanism and kinetics. Journal of the Electrochemical Society 2000;147(11):4013–22.
[57] Jiang SP, Zhang JP, Foger K. Deposition of chromium species at Sr-doped $LaMnO_3$ electrodes in solid oxide fuel cells II. effect on O_2 reduction reaction. Journal of the Electrochemical Society 2000;147(9):3195–205.

[58] Horita T, Xiong Y, Yoshinaga M, Kishimoto H, Yamaji K, Brito ME, et al. Determination of chromium concentration in solid oxide fuel cell cathodes: (La, Sr)MnO_3 and (La, Sr)FeO_3. Electrochemical and Solid-State Letters 2009;12(10):B146–9.
[59] Malzbender J, Steinbrech R, Singheiser L. Failure probability of solid oxide fuel cells. In: Ceramic engineering and science proceedings, vol. 26. American Ceramic Society; 2005. 293–298.
[60] Evans A, Hutchinson J. The thermomechanical integrity of thin films and multilayers. Acta Metallurgica et Materialia 1995;43(7):2507–30.
[61] ThyssenKrupp. Material data sheet no. 4046. URL http://thyssenkruppvdm.de/_pdf/Crofer22APU_e.pdf.
[62] Haynes International. Material data sheet no. h-3000h. URL http://www.haynesintl.com/pdf/h3000.pdf.